Evolution of iron minerals in a 100 years-old Technosol. Consequences on Zn mobility

Samuel Coussy, Sylvain Grangeon, Philippe Bataillard, Hicham Khodja, Nicolas Maubec, Pierre Faure, Christophe Schwartz, Robin Dagois

Evolution of iron minerals in a 100 years-old Technosol. Consequences on Zn mobility

Samuel Coussy[a*], Sylvain Grangeon[a], Philippe Bataillard[a], Hicham Khodja[b], Nicolas Maubec[a], Pierre Faure[c,d], Christophe Schwartz[e,f], Robin Dagois[a,c,d,e,f,g]

[a]*BRGM, 3 Avenue C. Guillemin BP 36009, 45060 ORLEANS Cedex 2, France*

[b]*LEEL, NIMBE, CEA, CNRS, Université Paris-Saclay, CEA Saclay 91191 Gif sur Yvette Cedex, France*

[c] *Laboratoire Interdisciplinaire des Environnements Continentaux, UMR 7360, CNRS, Vandœuvre-lès-Nancy, France*

[d] *Laboratoire Interdisciplinaire des Environnements Continentaux, UMR 7360, Université de Lorraine, Vandœuvre-lès-Nancy, France*

[e] *Laboratoire Sols et Environnement, UMR 1120, INRA, Vandœuvre-lès-Nancy, France*

[f] *Laboratoire Sols et Environnement, UMR 1120, Université de Lorraine, Vandœuvre-lès-Nancy, France*

[g] *ADEME, 20 Avenue du Grésillé, 49000 Angers*

E-mail adresses : s.coussy@brgm.fr, s.grangeon@brgm.fr, p.bataillard@brgm.fr, hicham.khodja@cea.fr, n.maubec@brgm.fr, pierre.faure@univ-lorraine.fr, christophe.schwartz@univ-lorraine.fr, robin.dagois@univ-lorraine.fr

[*] Corresponding author: Tél: +33 (0)2.38.64.38.43 Fax: +33 (0)2.38.64.37.60

1. Introduction

The industrial revolution in Europe that mainly took place in the 19th century and the concomitant growth of urban activities led to major changes in land use. Many new factories created at that time produced high quantities of wastes (smelter slags, brick residues, coke or coal) which were extensively used as backfill materials for levelling purposes (Lehmann and Stahr, 2007; Testiati et al., 2013; Nehls et al., 2013). Since that time, these wastes – often contaminated with trace metals – became the parental material of soils which developed thanks to alteration mechanisms due to mechanical, geochemical and biological processes. The newly formed soils are generally called Technosols or Anthropic Soils (Rossiter, 2007; WRB, 2006) because they contain at least 20% of man-made materials within the first 100 cm of the profile. Although contaminated, these materials present a pedologic interest since they fulfill several functions such as biomass production, storage-filtration and transformation of nutriments, trace elements and water, or formation of ecological niches (Morel et al., 2015). Furthermore, they are now a central compartment for urban re-developers who try to build the city in the city to preserve agricultural soils (Reeve et al., 2012). Understanding their fate is then of primary importance.

Pedogenesis processes generally take place in a timescale of thousands of years (Minasny et al., 2008; Salvador-Blanes et al., 2007) and involve structural changes in the soil profile, including incorporation and transformation of organic matter as well as mineral dissolution and/or precipitation (Costantini et al., 2006; Duchaufour, 1976; Néel et al., 2003). Technosols are often contaminated (e.g. Tsolova et al., 2014; Wanat et al., 2013) and, by analogy with natural and cultivated soils (Huot et al., 2013), pedogenetic evolution will certainly influence the speciation, mobility and

bioavailability of pollutants they contain. However, the kinetics and mechanisms of this evolution, as well as the consequences on pollutant speciation and mobility, are poorly constrained. It is currently admitted that the pedogenic processes occurring in Technosols are comparable to those occurring in natural soils, but can be accelerated due to the large thermodynamic disequilibria that can exist between the media of formation of the initial wastes and their new context of deposition (Séré et al., 2010; Leguédois et al., 2016). Coherently, several studies showed that early pedological transformations could be observed in Technosols, including oxidation, decarbonatation, secondary minerals precipitation, roots colonization and even humification in the first centimeters of the solum (Bataillard et al., 2008; Norra, 2006; Séré et al., 2010), although the first industrial activities started in Europe at maximum 200 years ago.

Investigation of the kinetics and mechanisms of Technosols formation can be performed by studying soil profiles where the deeper horizons are considered less evolved than the upper horizons submitted to climatic and biologic alteration (Brahy et al., 2000; Demattê and da Silva Terra, 2014; Egli et al., 2008). Hence, the deeper horizons in a selected Technosol profile could be considered as the parent material of the upper parts of the same profile. In this hypothesis, the characterization of the surface and deep horizons gives valuable information about the evolution of the parent material and the rates of alteration. However, because these materials have been deposited by human activities, it may be pointed out that these horizons may also differ due to their origin. This complicates the understanding of alteration impact on the chemistry of Technosols: each observation and analytical result must be interpreted with care.

In this study, the iron (Fe) status evolution is characterized during the early alteration processes occurring in a 100-year old Technosol, and its consequences in terms of Zn mobility are assessed. Fe, an ubiquitous element in natural and anthropic materials, is of special interest because Fe minerals (i) are reported to be reliable and well-accepted markers of soil evolution in soil sciences and (ii) control to a large extent the distribution and mobility of trace metals in soils, especially in the absence of Mn species (Bakker et al., 1996; Buol et al., 1973; Uzarowicz and Skiba, 2011). The slow transformation of primary Fe-bearing silicates in oxic and well-drained conditions lead to Fe depletion and precipitation of Fe (hydr)oxides such as goethite, lepidocrocite, ferrihydrite or magnetite (Bakker et al., 1996; Tawornpruek et al., 2006). Formation of free Fe (hydr)oxides can lead to the coating of soil particles with a thin film of these Fe (hydr)oxides (Ben-Dor et al., 2006). These mechanisms can compete with Fe complexation within the soil organic matter (Tipping et al., 2002).

For this study, a ~2m depth profile was sampled in a 100 years-old Technosol developed on backfills that contain significant concentrations of metals (e.g. Zn). Samples were characterized at different depths in order to quantify the changes in the chemical status of Fe, to identify the main mechanisms responsible for the mobility of trace elements such as Zn and to understand its consequences in terms of long-term potential emission by the Technosol.

2. Material and Methods

2.1. Field site description

The present study was conducted at the “Union” former industrial site (Tourcoing, France), located 50° 42’ 35” N, 3° 9’ 52” E. The site was occupied from the 19th century by several

types of industries, such as textile industries, breweries, smelters, chemical industries, transport companies, and a gas plant (Figure 1). A rail yard was built at the end of the 19th century at the north-west part of the site. Its reconversion for new activities is currently in progress.

A parcel of about 1,500 m² was chosen at the northern part of the former rail yard (Figure 1). The parcel shows a gentle slope from west to east, so that the railway (SW) is higher than the road (NE). The parcel is free of any buildings.

A total of 5 pits were dug in the parcel and briefly investigated. Only one pit was held up and kept for further investigation, whereas the remaining pits were filled up. Pit selection was done according to the following criteria:

- Absence of material recently backfilled at the surface (e.g. recent natural earthy material was found in some pits), and presence of aged backfills with evidences of vegetation development;

- Presence of a similar backfill material in depth which was not submitted to surface alteration.

2.2 Technosol profile dating

Investigations were carried out at the archives of the SNCF (French railways) to assess the probable date of setting of the backfills in the Technosol profile. A mail dating back October 6th, 1884 has indicated the establishment of a rail yard in the sector. Other archive documents pointed out the construction of a railway in 1889, other earthworks in 1897 and the construction of a special rail in 1898. Since then, no major works were done in the sector. The study of aerial photographs taken between 1950 and 2015 proved that the frame of the rail

yard always remained similar to the one represented in a map dating back 1898 (see supplementary material). Those photographs indicate also that the area where the Technosol is located has never been built since then. Thus, the area of study was not reworked for a century.

2.3.Technosol sampling and analyses

2.3.1. Soil profile sampling

The whole soil profile was sampled as a function of depth. Two types of samples were collected: composite samples (~1 kg per sample) for bulk analyses and samples representative of a given depth in the profile for punctual investigations (hereafter denominated “slices”).

Composite samples were taken within the following range of depth: 0-10 cm (samples A), 30-40 cm (samples C), 110-130 cm (samples E) and 175-185 cm (samples F). At each depth range, three replicates were taken on a same horizon (Figure 2). The samples were kept as it is in plastic bags and stored at 4 °C before analyses.

Soil slices were taken at 5 cm (LM1), 90 cm (LM2) and 180 cm (LM3) deep. The soil structure was preserved (non-destructive sampling using cylinders) and 3 thin sections embedded with epoxy resin were elaborated (final thickness: 30 µm).

2.3.2. Bulk analyses

In laboratory, after measuring the water content of the composite samples, the soil pH was measured in a 1:5 (volume fraction) suspension of soil in deionized water according to NF

ISO 10390. The total organic carbon content (TOC) was determined by dry combustion analysis according to NF ISO 10694. Organic carbon was analyzed after removal of carbonates by acidification using hydrochloric acid. Grain size distribution and total elemental concentrations were determined according to standardized methods (AFNOR, 1996, NF X 31–147). Cation exchange capacity (CEC) and exchangeable cations were measured with the cobaltihexamine chloride method (Orsini and Rémy, 1976), which can safely be used here, as samples contain little or no Fe(II)-bearing minerals (Hadi et al., 2016).

2.3.3 Leaching tests and selective dissolution

The release of trace elements was assessed by leaching of the composite samples. The 3 replicate samples taken at each depth range were tested. The samples were air dried and sieved (cut-off diameter of 2 mm). Then, the leaching tests were conducted at room temperature (20°C±2°C), in closed PTFE reactors with continuous stirring during 24h. A liquid/solid ratio of 10 was used with deionized water, corresponding to 10 g of dry sample in 100 mL water. The leachates were then filtrated (cut-off diameter of 0.45 µm) and analyzed by ICP-AES (major and trace elements such as Zn).

The Fe status was assessed by selective dissolution, using both Dithionite-Citrate-Bicarbonate (DCB) and pyrophosphate methods, done in parallel on aliquots. The methods used are detailed in Table 1. DCB selectively solubilizes pedogenic oxides and hydroxides (Mehra and Jackson, 1960). This method can solubilize crystalline Fe (hydr)oxides (hematite, goethite), non-crystalline Fe (hydr)oxides and Fe and Al organic complexes, whereas magnetite is slightly attacked and clays are unaffected. The pyrophosphate method was used to dissolve amorphous Fe(III), Fe(II) complexes and/or very poorly crystalline compounds (Pansu and Gautheyrou, 2006). Well-crystallized Fe (hydr)oxides like goethite and hematite are not

attacked and slightly ordered Fe (hydr)oxides are only slightly solubilized. Claff et al. (2010) tested the effect of these sequential chemical extractions on synthetic Fe minerals representative of some of those most abundant in the environment (e.g., akaganeite, ferrihydrite, goethite, hematite, jarosite, magnetite, pyrite and schwertmannite). They demonstrated that sodium pyrophosphate does not dissolve any of the tested minerals. The DCB procedure dissolves totally or significantly akaganeite, magnetite, goethite, hematite and ferrihydrite, and to a minor extent, jarosite.

2.3.4 Powder X-Ray diffraction analysis (XRD) on composite samples

The mineralogical assemblage of each composite sample was assessed by XRD, using a Siemens D5000 diffractometer with cobalt X-ray tube (CoKα radiation). The powdered composite samples were scanned with steps of 0.03°2θ and a counting time of 10s per step, in the 4-84°2θ angular range. Mineral identification and semi-quantitative determination of relative abundances of crystalline phases was performed using the software DIFFRAC plus EVA.

XRD patterns of composite samples were subjected to quantitative mineralogical analysis using the SIROQUANT^{TM} software. The quantification is based on the principles of Rietveld refinement (Rietveld, 1969). In addition to crystalline phases, SIROQUANT^{TM} was used to indirectly determine the amorphous phase content by spiking the samples with corundum internal standard. A precisely evaluated proportion of corundum by weight (target value of 10%) was added to the samples. The amorphous content was calculated by a routine within the SIROQUANT^{TM} program using a correction based on the weight-in proportion in the spike added prior to the XRD analysis.

2.3.5 Fe and Zn X ray absorption spectroscopy (XAS) analysis on composite samples

To complement selective dissolution for the study of Fe status, XAS analyses were carried out on composite samples. Moreover, the status of Zn, a recurrent trace element occurring in this Technosol, was also studied by XAS. The experiments were carried out at the Pacific Northwest Consortium Synchrotron Radiation Facility (PNCSRF) bending magnet beamline of the Advanced Photon Source (Argonne, IL, USA). The XAS spectra of composite samples were recorded, as well as those of reference minerals: natural hematite, natural 6L ferrihydrite, synthetic goethite and synthetic 2L and 6L ferrihydrite. Experiences of Zn co-precipitation and sorption onto ferrihydrite and goethite were also carried out. All ferrihydrite and goethite syntheses were performed using previously developed protocols (Schulze, 1984; Waychunas et al., 1993). X-ray absorption near-edge spectroscopy (XANES) spectra were systematically recorded. In addition, if the concentration of the element targeted (Fe or Zn) in the sample was sufficient, X-ray absorption fine structure spectroscopy (EXAFS) spectra were also collected. Fe XANES and EXAFS spectra were recorded in the range 6962-7912 ev, in transmission mode. The monochromator used was a double Si(111)–Si(220) crystal. A Fe foil was placed between the second and third ionization chamber for energy calibration. Each sample was scanned between 6 and 10 times, to increase the signal-to-noise ratio in the EXAFS region. All absorption spectra were calibrated according to the Fe K-edge position at 7128 eV corresponding to the maximum of the first derivative. EXAFS spectra were extracted using a spline function adjusted by minimizing the Fourier transform magnitude at radial distances <1 Å. EXAFS spectra were deglitched if necessary. Radial structure functions were obtained by Fourier transform of the EXAFS spectra, using a Kaiser-Bessel apodization function with a smoothing parameter of 3.0. Data reduction was done using the Iffefit software package (Ravel and Newville, 2005).

The Fe-bearing minerals building up the composite samples were determined by linear combination fit of the EXAFS spectra. The minimum number of components needed to reproduce the EXAFS spectra was determined by principal components analysis (Manceau et al., 2002) using the entire set of composite samples spectra. The minimum of the indicator function (0.017) shows that two components are needed to reproduce the whole set of spectra (Table 2).

Linear combinations were done between 3 and 11 $Å^{-1}$ in the EXAFS region. During the simulation, the following commonly used parameter was minimized:

$$R = \frac{\sum_{i=0}^{n}(data_i - fit_i)^2}{data^2} \times 100$$

Where *n* is the number of data point, $data_i$ is the data point number *i*, and fit_i is the fit value at point *i*.

The sum of the wt.% of each compound obtained after least square fitting calculations was also used as a goodness-of-fit parameter, since it should reach values close to 100 wt.% in a reliable reconstitution.

For Zn, XANES spectra were recorded in fluorescence mode (multi-element Canberra Ge detector), in the range 9511-10361 eV. Each sample was scanned 12 times and resulting spectra were averaged.

2.3.6 Nuclear microprobe investigations

Textural information was provided by nuclear microprobe analyses on thin sections made from samples collected at a precise depth. These experiments were performed using the

Laboratoire d'Etude des Eléments Légers nuclear microprobe in Saclay, France (Khodja et al., 2001). µ-PIXE and µ-RBS analyses were carried out on Fe-bearing phases pre-selected by SEM-EDS mapping. PIXE and RBS were used simultaneously to check the consistency of the results. Analyses were performed with 3.07 MeV 4He+ (Isaure et al., 2001) and oxygen quantified through resonant scattering. The size of the incident $^{4}He^{+}$ beam was approximately 4 x 4 μm^{2}. Prior analyses, both PIXE and RBS detection setups were calibrated with suitable standards.

All measurements were performed by electrostatically scanning the beam on pre-selected areas, and elemental contents from regions of interest were obtained by combining SIMNRA software (Mayer, 1997) for RBS and GUPIXWIN software (Campbell et al., 2010) for PIXE.

Major and trace elements were quantified by µ-PIXE and oxygen by µ-RBS. H and C cannot be quantified (only semi-quantification).

3. Results

3.1 Soil characteristics

The Technosol profile is made of several horizons of anthropogenic backfills from the surface to ~190 cm (Figure 2). These backfills consist in successions of homogeneous yellow-white pebbles horizons with heterogeneous backfills composed of a sandy brownish/darkish material mixed with bricks and concrete fragments. Coal and slag fragments are also found in these materials. Roots are present from the surface to ~170 cm depth. Below the backfill materials, quaternary yellow silts are observed. Brick fragments were found at the transition of the backfills and the quaternary silts (~200 cm). Below, the silts seem un-impacted by human activities.

The Technosol investigated here belongs either to the sandy loam class or to the silt loam class according to the FAO guideline for soil description (2006) because it contains 41-61% sand, 30-50% silt and only 8% clay at maximum (Table 3). Total organic carbon is abundant (> 20 g $100g^{-1}$) over the whole profile, probably due to the coal fragments found in the backfills. No particular biological investigation was performed, but it is noteworthy that no earthworm activity was observed in the profile.

pH and CEC are similar for the three replicate samples located on a same horizon, indicating that soil properties are homogeneous for a given depth. pH steadily increases with depth from 7.5 in surface sample to 8.5 in the deepest horizon. Oppositely, CEC decreases from ~23 meq 100 g^{-1} to 8-9 meq 100 g^{-1}. Fe concentrations vary from 6 to 2 wt. % in the profile, with no specific trend with depth. Such generally high Fe concentration cannot be quantitatively accounted for by the presence of crystalline Fe phases because hematite, the main Fe-bearing mineral detected by XRD, accounts for 0-3 wt. % of the mineral assemblage (Table 4). Thus, amorphous phases certainly contain Fe. Indeed, the mineralogical assemblage (Table 4) of the Technosol is mainly composed of an amorphous phase which can be formed by organic matter (Table 3) and contributes to 45-68 wt.% of the sample. Major minerals such as quartz and calcite are also present. In addition to hematite, accessory phases are constituted of phyllosilicates (illite, kaolinite) and sulphates (natrojarosite, syngenite). Such assemblage is typical of oxidized slags (Navarro and Martínez, 2010). Note that this Technosol contains significant amounts of trace metals such as Zn (Table 3), but also As and Pb (see total concentrations in supplementary material).

3.2 Evolution of the Fe status along the profile

Fe status was first assessed by selective dissolution, using DCB and pyrophosphate methods (Figure 3). The fraction of total Fe complexed to surfaces (including organic matter) is negligible, as only 0.5-2 % of total Fe content is extracted by pyrophosphate, with no dependence on depth in the profile. Contrastingly, 30-60 wt % of total Fe content is extracted by DCB, indicating the presence of "free" Fe ("free" Fe covers different status: Fe oxides and hydroxides as well as exchangeable Fe).

DCB results show that 20-30 % more of the total Fe is present as "free" Fe at the surface as compared to the bottom of the profile. Such higher Fe extraction near surface could be due to a depth-dependent mechanism of oxidation of primary Fe-bearing species. However, the studied materials already contain oxides inherited from the past industrial activities, either under crystallized (hematite) or glassy (amorphous phase) states, the latter having a typical structure of melting-quenching, coming from slags (Figure 4). To distinguish between Fe (hydr)oxides inherited from the past and (hydr)oxides newly precipitated since the deposit of the backfills, XAS was employed.

A first analysis of all XANES spectra, collected on samples originating from various depths, shows a high degree of similarity between them, witnessing generally similar Fe-bearing phases and Fe oxidation state over the whole profile (Figure 5a). In particular, the pre-edge features located at ~10–20 eV before the edge jump and which are particularly sensitive to the Fe oxidation state are similar for all samples, with a maximum located at ~7114.3 eV, indicative of the predominance of Fe(III) species throughout the profile (Sundman et al., 2014). Upon closer examination, however, the first derivatives shows a change with depth in the respective contributions of two inflexion points at 7124 eV and 7128 eV. As the 7124 eV and 7128 eV contributions are respectively attributable to Fe(II) and Fe(III) (Sundman et al.,

2014), such variations are attributed to a slightly higher contribution of Fe(II) in the lower part of the profile and not to statistical fluctuations because the first derivative of XANES spectra of two samples from a same horizon showed similar contributions of each inflexion point (Figure 5b and c). SEM-EDS observation of a sample taken at 175-185 cm depth (sample F1) evidenced the regular presence of particles of ~10 µm in width and containing solely Fe and S (Figure 6). These Fe sulphides could be at the origin of the slightly higher Fe(II) signal observed in depth by XANES. They were not detected by XAS and XRD (see Table 4, Figure 5 and Figure 7) because of their minor abundance as compared to the other Fe-bearing phases.

The mineralogy of the Fe-bearing phases was further assessed by least-square fitting of EXAFS spectra. Assuming that the evolution as a function of depth is due to weathering, and assuming that the sample collected in the bottom is representative of the lowest degree of weathering, samples from the bottom to the top can be described as a mixture of the sample from the bottom, plus additional component(s) that were formed during weathering. From PCA analysis (see above), only two components are required to describe the whole system. Following this approach, simulation of the spectra from samples collected in the surface horizon (A1) and at intermediate depth (E1) was performed, assuming that they could be described as a weighted sum of sample from the bottom (F1), plus an additional mineral that results from weathering. For the surface sample, the best fit (Figure 7) was obtained with 77% of sample from the bottom plus 25% of ferrihydrite. This is consistent with the DCB extraction results, as the increase in the DCB-extractable fraction between depth (sample F) and surface (sample A) was equal to 20-30%. Note that the sum of the weighted fraction of the two components is close to 1, thus reinforcing the confidence in simulation results. For the intermediate sample, the best fit (Figure 7) was obtained with 85% of sample from the bottom plus 15% of ferrihydrite, confirming that ferrihydrite proportion decreases with depth.

These results indicate a change in the status of Fe along depth. An assumption is that this change could influence the speciation of trace elements. The specific case of Zn is addressed in this paper since it is present in significant concentrations (up to 4,000 µg g^{-1}) in the profile. The status of Zn was investigated in relation with Fe but also with Mn status since Mn-bearing phases can also be major scavengers of trace metals (Grangeon et al., 2012; Koschinsky and Hein, 2003; Manceau et al., 2000; Peacock and Sherman, 2007).

3.3 Evolution of the Zn status along the Technosol profile and assessment of Zn mobility

The evolution of Zn speciation was first assessed using Zn-K edge XANES analysis of composite samples, as it provides an integrating view. Data are presented as a function of depth for two sets of replicate samples (Figure 8).

The XANES spectra are similar for each replicate samples, indicating that Zn speciation is similar at any location at the same depth. Contrastingly, changes with depth are observed. The contribution at 9668.5 eV is higher in the deepest samples (F1 and F3) whereas the peak at 9665.5 eV is more pronounced in the surface samples (A, C and E). In Zn-ferrihydrite reference sample, the main contribution is located at 9665.5 eV. According to Cismasu et al. (2013) and Waychunas et al. (2003), the position of the edge is indicative of Zn coordination. When coordination is octahedral, the XANES spectrum only has one well defined edge, whereas when coordination is tetrahedral, the XANES presents several maxima, as it is the case here. Indeed, all XANES spectra have two maxima at ~9665.5 eV and ~9668.5 eV. Thus, in presently studied samples, Zn coordination is tetrahedral. With increasing depth, the intensity of the maximum at ~9665.5 eV relative to that at ~9668.5 eV evolves, and is lowest at the maximum depth. As discussed by Waychunas et al., 2003, this is indicative of an increasing number of heavy (*e.g.* Fe) scattering atoms around Zn, and thus of sorption to

349 better-crystallized phases. Consequently, in the deeper horizons, Zn is associated to phases
350 having a higher degree of crystallinity than in the surface horizons. This demonstrates that the
351 weathering processes during soil evolution influence Zn speciation, but do not necessarily
352 relate to Zn mobility as, for example, it gives no information on the solubility of the sorbing
353 phases. To study Zn mobility, and to compare this element to other major elements, leaching
354 of the composite samples was performed. The results indicate that Fe, Mn and Zn are all very
355 little labile throughout the whole profile (Figure 9). Thus, all these elements probably are
356 under the form of mineral phases (Fe, Mn) or strongly bound to mineral phases (Zn), which
357 are determined in the following.

358 Zn content was investigated first using pyrophosphate extraction, which showed that the
359 fraction of total complexed Zn, partly borne by organic matter is, within uncertainties,
360 constant and equal on average to 18% (Figure 10a). Thus, although organic matter is a
361 significant Zn reservoir, it does not represent the only Zn bearing-phase. The Zn content of
362 the DCB-soluble fraction was investigated next. Fe extraction yields are presented here above
363 (Figure 4b), and those from Mn and Zn are shown in Figure 10b. Both Zn and Mn are
364 significantly affected by DCB extraction. Zn extraction yield (35% on average) is, within
365 uncertainties, constant over the whole profile, while Mn has a slightly different behavior, 69 ±
366 4 % being extracted in the first 40 cm depth, 51 ± 6 % at 120 cm depth and 62 ± 4 % at 180
367 cm depth (Figure 10b). As DCB solubilizes Mn (hydr)oxides (Mehra and Jackson, 1960), it
368 can be concluded that Mn is mainly present in the profile as discrete Mn (hydr)oxide(s). Here
369 above, it was shown that Fe is also mainly present as (hydr)oxides. These two (hydr)oxides
370 can potentially bear Zn, which is confirmed by the tetrahedral coordination of Zn assessed by
371 EXAFS. Note that, although within uncertainties, the fraction of Zn extracted by DCB might
372 increase with depth. However, as Zn concentration in the deepest sampling point (175-185 cm
373 depth) is 10 times lower that in the surface horizon (0-10 cm depth), and even 26 times lower

than in the sampling point just above (110-130 cm depth), a small quantity of Fe and Mn (hydr)oxides that would have migrated from the upper horizons (or a limited contamination, for example during sampling) may have led to such apparent slight change extraction yield. According to this assumption, Zn is probably associated in depth with the Fe (hydr)oxides originally present in the backfills, but also with the newly formed Fe (hydr)oxides at the surface of the profile that would have migrated.

To summarize, in this profile and on average, less than 0.1 % of total Zn is H_2O-extractable, up to 18 % of total Zn would be bound to organic matter, 35 % of total Zn would be adsorbed onto Fe/Mn (hydr)oxides, and about 47 % of total Zn is present under a residual form (that cannot be accessed with any of the extractant used here). To better constrain this distribution, µ-PIXE and µ-RBS are now used with a twofold aim: first, cross-check results from chemical extraction and in particular the association between Zn and Fe/Mn pedogenic (hydr)oxides, second, determine the nature of the residual form. These analyses were performed on sample LM2 sample (90 cm depth).

The association between Zn and Fe (hydr)oxides could be straightforwardly and regularly observed, as exemplified in Figure 11. The grain showed in this image is made of coal, with a Fe coating having a size of about 50 µm on the edge. The morphology suggests that the Fe (hydr)oxide is a secondary phase and was formed during soil evolution. Using quantitative analyses performed two regions of interest (ROI – Table 5), this Fe (hydr)oxide is probably the ferrihydrite identified using EXAFS spectroscopy, since Fe/O atomic ratios in the two ROIs (respectively 0.42 and 0.51) are lower than the theoretical Fe/O ratio of hematite (0.66), but are consistent with Fe/O ratio of ferrihydrite (theoretical value from 0.42 to 0.57 depending on the hydration state). Table 5 indicates also that Zn/Fe atomic ratio could reach up to 17%, which further confirms that ferryhydrite is a very efficient sink for metallic trace elements.

399 The nature of the Zn-bearing phase forming the residual phase was found to be complex, as
400 demonstrated in Figure 12 and Table 6, where complex associations between Zn, Mn, Fe, S
401 and O could be quantified. The quantitative analysis carried out in some regions of interest
402 (ROI) show various elemental proportions (Table 6). The grain is composed of different Fe-
403 compounds: Fe (hydr)oxides (ROI 3,4,6) and Mn, Zn, Fe-bearing sulphates (ROI 1 and 5).
404 Interestingly, these latter are likely a mix of sulphides undergoing oxidation and forming
405 sulphates (see the white arrow in Figure 12 b and c), since the S/O ratio of 0.42 (ROI 1 and 5),
406 are higher than the expected ratio in a sulphate (0.25). It is interesting to note that the external
407 part of the grain (ROI 3 and 4) do not contain sulphur. It is only composed of Fe (hydr)oxides,
408 and contain less than 0.2 atomic percent of Zn. Fe/O atomic ratio calculated for all the Fe
409 (hydr)oxides (see Table 6) range from 0.45 to 0.48. These values are lower than Fe/O ratio of
410 hematite (0.66) and goethite (0.5), but are consistent with Fe/O ratio of ferrihydrite (0.42-0.57
411 depending on the hydration state).

412

413 4. Discussion

414 The study of the Fe status by several methods of investigation throughout the Technosol
415 profile indicates that (i) Fe is mainly under Fe(III) form, with a contribution of Fe(II) in the
416 deeper samples, (ii) some Fe species inherited from the past have been oxidized and
417 secondary minerals are constituted of Fe-bearing sulphates (jarosite) and Fe (hydr)oxides, (iii)
418 Fe(III) is mainly under the form of ferrihydrite, as evidenced by XAS, µ-PIXE and µ-RBS
419 (iv) 20 to 30% more Fe (hydr)oxides are present in the surface than in depth. Ferrihydrite
420 forms coatings surrounding different grains of the Technosol, in consistence with a
421 neoformation induced by weathering processes. Previous studies have shown that in slags,
422 secondary minerals formed by oxidation can be present as coatings on surfaces and as

precipitates of various phases such as amorphous Fe, Al (hydr)oxides, chalcanthite, siderotil, jarosite, brochantite or gypsum (Navarro and Martínez, 2010; Piatak et al., 2004). Fe sulphate and Fe (hydr)oxides are both secondary minerals formed by oxidation of Fe-bearing sulphides (Blowes et al., 2005). Such reaction typical of acid mine drainage can be encountered in all kind of wastes containing sulphides. In the present study, this assumption is consistent with the sulphates found by XRD and µ-PIXE, as well as the Fe sulphides encountered in depth (see Figure 6 above). However, the pH remains near-neutral to slightly basic since the net-acid-generating potential was probably exceeded by the net-neutralizing potential due to a low sulphide/neutralizing minerals ratio (e.g. Plante et al., 2011). Thus, the main evolution driver of this 100 years-old Technosol is oxidation, which affects the Fe status, the CEC and the related trace elements mobility. The presence of free Fe at the surface of this Technosol is of interest since it provides the soil with an efficient trace metals sink and since such Fe is easily accessible to plants (Pansu and Gautheyrou, 2006). According to Navarro and Martínez (2010), the formation of secondary phases (*e.g.* jarosite, gypsum, goethite, ferrihydrite) may control the distribution of trace elements in the pore water and the degree to which they are mobilized into the environment. Dissolution of primary minerals leads to trace elements release in pore water solution. These trace elements can precipitate to form secondary minerals, or can be sorbed onto these secondary minerals.

In the studied Technosol, XANES revealed that Zn has tetrahedral coordination and is sorbed to phases of increasing crystallinity when depth increases. This could indicate that the amorphous Fe (hydr)oxides inherited from the past are slightly more crystalline than the newly formed Fe (hydr)oxides at the surface. Soil formation on such material does not induce a dramatic increase of Zn solubility since efficient scavengers are concomitantly formed in the system. Zn-bearing phases identified in the present study are: complex Fe, Mn, Zn sulphides, which may be the primary Zn-bearing phase, sulphates which may be the oxidation product of

448 the sulphides, organic matter, and ferrihydrite. On the contrary, no Zn-bearing Mn
449 (hydr)oxides were found, even if there are known to be important sinks of trace elements such
450 as Zn.

451 The assumption that the deeper horizons are the parent material in this Technosol profile is
452 difficult to prove since the characteristics of the original material at the time of backfill
453 deposit are unknown. However, the observed evolution of Fe mineralogy with depth, as well
454 as Zn speciation change and CEC decrease with depth, is a clue for the validity of this
455 assumption.

456 This study also highlights that DCB selective extraction method is relevant to investigate Fe
457 status in a Technosol, since the relative proportion of “free” Fe - mainly Fe (hydr)oxides -
458 quantified by DCB (20-30% in surface) is similar to the ones estimated by EXAFS linear
459 combination fitting (25% in surface). DCB is also interesting to assess the relations between
460 all the “free” Fe species and trace elements such as Zn, even if the concentrations of Zn bound
461 to Fe (hydr)oxides are probably underestimated by this extraction. Indeed, dithionites are
462 labile compounds which undergo rapid disproportionation in aqueous solution due to their
463 sensitivity to oxygen. This decomposition is rapid at pH < 5.5 but also occur at neutral and
464 basic pH (de Carvalho and Schwedt, 2001). It produces mainly thiosulphate and bisulphite
465 which will be the final product of the disproportionation. But intermediate sulphide and
466 elemental sulfur, playing a catalytic role, are also encountered in solution as minor
467 decomposition products (de Carvalho and Schwedt, 2001; Wayman and Lem, 1970).
468 Dissolved sulphide can react with Zn to precipitate ZnS during DCB extraction (Rao et al.,
469 2008). This would explain the gap between DCB results which show that only 35% of total
470 Zn is dissolved whereas XANES and nuclear microprobe indicate a major contribution of Zn
471 associated with ferrihydrite.

In the future, this Technosol will potentially evolve again because some phases are not thermodynamically stable in conditions of pH observed here. For instance, jarosite is known to be stable at pH<3 (Blowes et al., 2005), whereas the pH in the Technosol is near-neutral to slightly basic. Moreover, the input of organic matter at the surface based on organic C determination, is slightly visible after 100 years of evolution. Pyrophosphate extractions have shown that Fe and Zn are variably complexed to surfaces (including organic matter). However, the pyrophosphate extract does not only determine organic forms but also dissolves poorly crystalline mineral phases (e.g. Kaiser and Zech, 1996). Mineralogical investigations confirmed that Fe and Zn are not complexed on coal which is the most abundant carbon phase of the Technosol. Indeed, Fe and Zn were not observed at the surface of the coal grains (see Figure 11). Though, other clues of evolution are visible in the studied Technosol. CEC is higher near surface and could indicate that the soil surface reached a higher evolution stage than the deeper horizons, either due to weathering or to bioturbation. Organic matter will probably play an important role in the future on major and trace element speciation.

5. Conclusions and environmental implications

Technosols are highly heterogenous and widely differ from one place to another because of the variety of their constitutive man-made materials. In this study, a Technosol made of smelter slags, i.e. containing high amounts of coal and Fe (hydr)oxides was characterized. The results indicate that 100 years of soil evolution has led to the precipitation of secondary minerals (including Fe (hyrdr)oxides and Fe sulphates) at the surface of the profile. This behavior is similar to pedogenic processes occurring in natural soils, but other specific evolutions due to large thermodynamic disequilibrium can be highlighted, in particular sulphide oxidation and sulphate precipitation. This specific behavior of Technosols over time

can be generalized to all kinds of Technosols, even if the final reaction products are not similar. Such evolution influences pollutants mobility including trace elements release. In this specific study, Technosol evolution does not induce a dramatic increase of Zn solubility since efficient scavengers are concomitantly formed in the system. However, this behavior is not generic and will depend on the type of Technosol and on the secondary minerals formed as well as on the nature and amount of organic matter. If the trace metals sinks are not abundant and/or efficient, this could potentially represent a risk of mobilization of trace metals. This must be carefully examined through case studies.

Acknowledgments

The authors would like to acknowledge the French Environmental Agency (Ademe; Hélène Roussel) for their financial support (REITERRE research program) and advices through this work. S.G. acknowledges partial funding by the ANR (NACRE—ANR-14-CE01-0006). The XAFS experiments were performed at the Advanced Photon Source (sector 20). Sector 20 facilities at the Advanced Photon Source, and research at these facilities, are supported by the US Department of Energy - Basic Energy Sciences, the Canadian Light Source and its funding partners, the University of Washington, and the Advanced Photon Source. Use of the Advanced Photon Source, an Office of Science User Facility operated for the U.S. Department of Energy (DOE) Office of Science by Argonne National Laboratory, was supported by the U.S. DOE under Contract No. DE-AC02-06CH11357. Special thanks to Robert Gordon and Michael Pape, who helped with the experiments at the beamline.

References

519 Bakker, L., Lowe, D.J., Jongmans, A.G., 1996. A micromorphological study of pedogenic
520 processes in an evolutionary soil sequence formed on Late Quaternary rhyolitic tephra
521 deposits, North Island, New Zealand. Quaternary International 34–36(0), 249-261.

522 Bataillard, P., Grangeon, S., Quinn, P., Mosselmans, F., Lahfid, A., Wille, G., Joulian, C.,
523 Battaglia-Brunet, F., 2014. Iron and arsenic speciation in marine sediments undergoing a
524 resuspension event: the impact of biotic activity. Journal of Soils and Sediments 14(3), 615-
525 629.

526 Bataillard, P., Guérin, V., Lions, J., Girondelot, B., Laboudigue, A., van der Lee, J., Raepsaet,
527 C., Gallien, J., 2008. Mobilité des éléments traces dans un Anthroposol développé sur des
528 sédiments de curage fortement contaminés - 1 - Migration à l`échelle du profil. Étude et
529 Gestion des Sols, pp. 7-18.

530 Ben-Dor, E., Levin, N., Singer, A., Karnieli, A., Braun, O., Kidron, G.J., 2006. Quantitative
531 mapping of the soil rubification process on sand dunes using an airborne hyperspectral sensor.
532 Geoderma 131(1–2), 1-21.

533 Blowes, D.W., Ptacek, C.J., Jambor, J.L., Weisener, C.G., 2005. The geochemistry of acid
534 mine drainage. Treatise on Geochemistry, Vol 9: Environmental Geochemistry, 149-204.

535 Brahy, V., Deckers, J., Delvaux, B., 2000. Estimation of soil weathering stage and acid
536 neutralizing capacity in a toposequence Luvisol–Cambisol on loess under deciduous forest in
537 Belgium. European Journal of Soil Science 51(1), 1-13.

538 Buol, S., Hole, F., McCracken, R., 1973. Soil genesis and classification. The Iowa State
539 University Press, Ames, pp. 360.

Campbell, J.L., Boyd, N.I., Grassi, N., Bonnick, P., Maxwell, J.A., 2010. The Guelph PIXE software package IV. Nuclear Instruments and Methods in Physics Research Section B: Beam Interactions with Materials and Atoms 268(20), 3356-3363.

Cismasu, A.C., Levard, C., Michel, F.M., Brown Jr, G.E., 2013. Properties of impurity-bearing ferrihydrite II: Insights into the surface structure and composition of pure, Al- and Si-bearing ferrihydrite from Zn(II) sorption experiments and Zn K-edge X-ray absorption spectroscopy. Geochimica et Cosmochimica Acta 119, 46-60.

Claff, S.R., Sullivan, L.A., Burton, E.D,, Bush, R.T., 2010. A sequential extraction procedure for acid sulphate soils: partitioning of iron. Geoderma 155, 224–230.

Costantini, E.A.C., Lessovaia, S., Vodyanitskii, Y., 2006. Using the analysis of iron and iron oxides in paleosols (TEM, geochemistry and iron forms) for the assessment of present and past pedogenesis. Quaternary International 156–157, 200-211.

de Carvalho, L.M., Schwedt, G., 2001. Polarographic determination of dithionite and its decomposition products: kinetic aspects, stabilizers, and analytical application. Analytica Chimica Acta 436(2), 293-300.

Demattê, J.A.M., da Silva Terra, F., 2014. Spectral pedology: A new perspective on evaluation of soils along pedogenetic alterations. Geoderma 217–218, 190-200.

Duchaufour, P., 1976. Dynamics of organic matter in soils of temperate regions: Its action on pedogenesis. Geoderma 15(1), 31-40.

Egli, M., Merkli, C., Sartori, G., Mirabella, A., Plötze, M., 2008. Weathering, mineralogical evolution and soil organic matter along a Holocene soil toposequence developed on carbonate-rich materials. Geomorphology 97(3–4), 675-696.

562 FAO, 2006. Guidelines for soil description. Food and Agriculture Organization of the United
563 Nations, Rome.

564 Grangeon, S., Manceau, A., Guilhermet, J., Gaillot, A.-C., Lanson, M., Lanson, B., 2012. Zn
565 sorption modifies dynamically the layer and interlayer structure of vernadite. Geochimica Et
566 Cosmochimica Acta 85, 302-313.

567 Hadi, J., Tournassat, C., Lerouge, C., 2016. Pitfalls in using the hexaamminecobalt method
568 for cation exchange capacity measurements on clay minerals and clay-rocks: Redox
569 interferences between the cationic dye and the sample. Applied Clay Science 119, Part 2, 393-
570 400.

571 Huot, H., Simonnot, M.-O., Marion, P., Yvon, J., De Donato, P., Morel, J.-L., 2013.
572 Characteristics and potential pedogenetic processes of a Technosol developing on iron
573 industry deposits. Journal of Soils and Sediments 13(3), 555-568.

574 Ingerslev, M., 1997. Effects of liming and fertilization on growth, soil chemistry and soil
575 water chemistry in a Norway spruce plantation on a nutrient-poor soil in Denmark. Forest
576 Ecology and Management 92(1–3), 55-66.

577 Isaure, M.P., Laboudigue, A., Manceau, A., Sarret, G., Tiffreau, C., Trocellier, P., 2001.
578 Characterisation of zinc in slags originated from a contaminated sediment by coupling μ-
579 PIXE, μ-RBS, μ-EXAFS and powder EXAFS spectroscopy. Nuclear Instruments and
580 Methods in Physics Research Section B: Beam Interactions with Materials and Atoms 181(1–
581 4), 598-602.

582 Kaiser, K., Zech, W., 1996. Defects in estimation of aluminium in humus complexes of
583 podzolic soils by pyrophosphate extraction. Soil Science 161, 452-458.

584 Khodja, H., Berthoumieux, E., Daudin, L., Gallien, J.-P., 2001. The Pierre Süe Laboratory
585 nuclear microprobe as a multi-disciplinary analysis tool. Nuclear Instruments and Methods in
586 Physics Research Section B: Beam Interactions with Materials and Atoms 181(1–4), 83-86.

587 Koschinsky, A., Hein, J.R., 2003. Uptake of elements from seawater by ferromanganese
588 crusts: solid-phase associations and seawater speciation. Marine Geology 198(3-4), 331-351.

589 Leguédois, S., Séré, G., Auclerc, A., Cortet, J., Huot, H., Ouvrard, S., Watteau, F., Schwartz,
590 C., Morel, J.L. 2016. Modelling pedogenesis of Technosols. Geoderma, 262, 199-212.

591 Lehmann, A., Stahr, K., 2007. Nature and significance of anthropogenic urban soils. Journal
592 of Soils and Sediments 7(4), 247-260.

593 Manceau, A., Lanson, B., Schlegel, M.L., Harge, J.C., Musso, M., Eybert-Berard, L.,
594 Hazemann, J.L., Chateigner, D., Lamble, G.M., 2000. Quantitative Zn speciation in smelter-
595 contaminated soils by EXAFS spectroscopy. American Journal of Science 300(4), 289-343.

596 Manceau, A., Marcus, M.A., Tamura, N., 2002. Quantitative Speciation of Heavy Metals in
597 Soils and Sediments by Synchrotron X-ray Techniques. Reviews in Mineralogy and
598 Geochemistry 49(1), 341-428.

599 Mayer, M., 1997. SIMNRA User's Guide. Report IPP 9/113, Max-Planck-Institute für
600 Plasmaphysik, Garching, Germany.

601 Mehra, O.P., Jackson, M.L., 1960. Iron oxide removal from soils and clays by a dithionite-
602 citrate system buffered with sodium bicarbonate. Clays and Clay Minerals, pp. 317-327.

603 Minasny, B., McBratney, A.B., Salvador-Blanes, S., 2008. Quantitative models for
604 pedogenesis — A review. Geoderma 144(1–2), 140-157.

605 Morel, J., Chenu, C., Lorenz, K., 2015. Ecosystem services provided by soils of urban,
606 industrial, traffic, mining, and military areas (SUITMAs). Journal of Soils and Sediments
607 15(8), 1659-1666.

608 Navarro, A., Martínez, F., 2010. The use of soil-flushing to remediate metal contamination in
609 a smelting slag dumping area: Column and pilot-scale experiments. Engineering Geology
610 115(1–2), 16-27.

611 Néel, C., Bril, H., Courtin-Nomade, A., Dutreuil, J.-P., 2003. Factors affecting natural
612 development of soil on 35-year-old sulphide-rich mine tailings. Geoderma 111(1–2), 1-20.

613 Nehls, T., Rokia, S. , Mekiffer, B., Schwartz, C., Wessolek, G., 2013. Contribution of bricks
614 to urban soil properties. Journal of Soils and Sediments 13(3), 575-584.

615 Norra, S., 2006. Urban Soil Science on the 18th WCSS. Journal of Soils and Sediments 6(3),
616 189-189.

617 Orsini, L., Rémy, J.C., 1976. The use of the chloride of cobaltihexamine for the simultaneous
618 determination of the exchange capacity and exchangeable bases in soils. Sci. Sol, pp. 269-
619 275.

620 Pansu, M., Gautheyrou, J., 2006. Mineralogical Separation by Selective Dissolution. In:
621 Springer (Ed.), Handbook of soil analysis. Mineralogical, Organic and Inorganic Methods.,
622 pp. 167-219.

623 Peacock, C.L., Sherman, D.M., 2007. Crystal-chemistry of Ni in marine ferromanganese
624 crusts and nodules. American Mineralogist 92(7), 1087-1092.

625 Piatak, N.M., Seal Ii, R.R., Hammarstrom, J.M., 2004. Mineralogical and geochemical
626 controls on the release of trace elements from slag produced by base- and precious-metal
627 smelting at abandoned mine sites. Applied Geochemistry 19(7), 1039-1064.

628 Plante, B., Benzaazoua, M., Bussière, B., 2001. Predicting Geochemical Behaviour of Waste
629 Rock with Low Acid Generating Potential Using Laboratory Kinetic Tests. Mine Water and
630 the Environment 30, 2–21.

631 Rao, C.R.M., Sahuquillo, A., Sanchez, J.F.L., 2008. A review of the different methods applied
632 in environmental geochemistry for single and sequential extraction of trace elements in soils
633 and related materials. Water Air and Soil Pollution 189(1-4), 291-333.

634 Ravel, B., Newville, M., 2005. ATHENA, ARTEMIS, HEPHAESTUS: data analysis for X-
635 ray absorption spectroscopy using IFEFFIT. Journal of Synchrotron Radiation 12(4), 537-
636 541.

637 Reeve, A., Desha, C., Hargroves, C., Newman, P., Hargreaves, D., 2012. A basis for a
638 pragmatic inquiry into the policy considerations related to the increased application of
639 Biophilic Urbanism, 11th Urban Environment Symposium, pp. 16-19.

640 Rietveld, H., 1969. A profile refinement method for nuclear and magnetic structures. Journal
641 of Applied Crystallography 2(2), 65-71.

642 Rossiter, D.G., 2007. Classification of urban and industrial soils in the world reference base
643 for soil resources. Journal of Soils and Sediments 7(2), 96-100.

644 Salvador-Blanes, S., Minasny, B., McBratney, A.B., 2007. Modelling long-term in situ soil
645 profile evolution: application to the genesis of soil profiles containing stone layers. European
646 Journal of Soil Science 58(6), 1535-1548.

Schulze, D., 1984. The influence of aluminum on iron oxides. VIII. Unit-cell dimensions of AI-substituted goethites and estimation of A1 from them. Clays Clay Miner 32, 27-39.

Séré, G., Schwartz, C., Ouvrard, S., Renat, J.C., Watteau, F., Villemin, G., Morel, J.L., 2010. Early pedogenic evolution of constructed Technosols. Journal of Soils and Sediments 10(7), 1246-1254.

Sundman, A., Karlsson, T., Laudon, H., Persson, P., 2014. XAS study of iron speciation in soils and waters from a boreal catchment. Chemical Geology 364, 93-102.

Tawornpruek, S., Kheoruenromne, I., Suddhiprakarn, A., Gilkes, R.J., 2006. Properties of red Oxisols on calcareous sedimentary rocks in Thailand. Geoderma 136(3–4), 477-493.

Testiati, E., Parinet, J., Massiani, C., Laffont-Schwob, I., Rabier, J., Pfeifer, H.-R., Lenoble, V., Masotti, V., Prudent, P., 2013. Trace metal and metalloid contamination levels in soils and in two native plant species of a former industrial site: Evaluation of the phytostabilization potential. Journal of Hazardous Materials 248–249, 131-141.

Tipping, E., Rey-Castro, C., Bryan, S.E., Hamilton-Taylor, J., 2002. Al(III) and Fe(III) binding by humic substances in freshwaters, and implications for trace metal speciation. Geochimica et Cosmochimica Acta 66(18), 3211-3224.

Tsolova, V.T., Hristova, M.B., Borras, J.B., Pascual, N.R., Banov, M.D., 2014. Pb, Cu and Zn geochemistry in reclaimed soils (Technosols) of Bulgaria. Journal of Geochemical Exploration 144, 337-344.Uzarowicz, Ł., Skiba, S., 2011. Technogenic soils developed on mine spoils containing iron sulphides: Mineral transformations as an indicator of pedogenesis. Geoderma 163(1–2), 95-108.

Wanat, N., Austruy, A., Joussein, E., Soubrand, M., Hitmi, A., Gauthier-Moussard, C., Lenain, J.F., Vernay, P., Munch, J.C., Pichon, M., 2013. Potentials of Miscanthus x giganteus grown on highly contaminated Technosols. Journal of Geochemical Exploration 126, 78-84.Waychunas, G.A., Fuller, C.C., Davis, J.A., Rehr, J.J., 2003. Surface complexation and precipitate geometry for aqueous Zn(II) sorption on ferrihydrite: II. XANES analysis and simulation. Geochimica et Cosmochimica Acta 67(5), 1031-1043.

Waychunas, G.A., Rea, B.A., Fuller, C.C., Davis, J.A., 1993. Surface chemistry of ferrihydrite: Part 1. EXAFS studies of the geometry of coprecipitated and adsorbed arsenate. Geochimica et Cosmochimica Acta 57(10), 2251-2269.

Wayman, M., Lem, W.J., 1970. Decomposition of aqueous dithionite. Part II. A reaction mechanism for the decomposition of aqueous sodium dithionite. Canadian Journal of Chemistry 48(5), 782-787.

WRB, 2006. World Reference Base for Soil Resource 2006, 2nd ed. World Resources Report, 103. FAO, Rome.

Tables

Table 1 Summary of selective dissolution procedures (from Bataillard et al., 2014)

Fraction	Reagent	Shaking time and temperature
Citrate-bicarbonate-dithionite (CBD)	0.3 M Na Citrate pH 7.3+$Na_2S_2O_4$+NaCl saturated solution	1 g DM moist sediment/10 ml 0.3 M NaCitrate pH 7.3+0.4 g $Na_2S_2O_4$+2 mL NaCl saturated solution Heat 15 min 80 °C Centrifugation 5 min at about 3,000 g Repeated twice
Sodium pyrophosphate	0.05 M $Na_4O_7P_2$	2 g DM moist sediment/200 ml $Na_4O_7P_2$ Agitation 16 H, 20 °C±5 °C. Centrifugation 20 min 18,000 rpm

Table 2: Results of the principal component analysis on the 8 composite sample spectra. The minimum of the indicator (IND) function shows that two components are needed to reproduce the whole set of spectra.

Component	**Eigenvalue**	**IND[a]**
1	13.7	0.018
2	1.7	0.017
3	0.9	0.022
4	0.8	0.028
5	0.6	0.040
6	0.4	0.085
7	0.4	0.32

[a]Indicator function

Table 3. Technosol characteristics and properties (ND: not determined)

Soil sample	Depth (cm)	Texture (%)			pH	Total organic carbon (g $100g^{-1}$)	CEC (meq $100g^{-1}$)	Total Fe (wt. %)	Total Mn (wt. %)	Total Zn (mg kg^{-1})
		Clay	Silt	Sand						
A1	0-10	8	50	42	7.5	25	22.8	4.5	0.06	1817
A2			ND		7.6	26.3	21.3	4.8	0.06	1245
A3			ND		7.7	24.9	20.1	4.2	0.06	1365
C1	30-40	8	31	61	7.8	35.3	15.6	5.3	0.06	656
C2			ND		8.2	38.0	14.8	5.3	0.06	552
C3			ND		8.2	28.8	14.3	3.9	0.06	928
E1	110-130	8	39	53	8.3	38.9	10.1	4.2	0.06	4021
E2			ND		8.3	27.4	10.7	4.5	0.09	3677
E3			ND		8.4	25.3	10.9	5.3	0.12	4740
F1	175-185	5	30	65	8.4	31.8	9.5	2.2	0.03	760
F2			ND		8.5	48.7	8.1	2.0	0.03	180
F3			ND		8.5	46.8	9.2	2.0	0.03	312

Table 4. Relative proportion of crystalline minerals in the bulk composite samples of the Technosol profil estimated by Rietveld analysis (ND: not detected)

Mineral proportion (wt.%)[a]	**A1**	**C1**	**E1**	**F1**
Quartz	31	14	15	23
Calcite	4	2	1	5
Albite	2	1	<1	1
Microcline	1	<1	<1	1
Dolomite	4	1	1	ND
Natrojarosite	<1	<1	ND	1
Hematite	2	3	<1	1
Mullite	3	3	2	1
Syngenite	1	<1	<1	<1
Illite/mica	4	4	10	6
Kaolinite	3	4	4	1
Amorphous phase	45	68	67	60

[a]Error on these results: +/- 5 wt%

Table 5. Quantitative elementary results obtained by µ-PIXE and µ-RBS on two regions of interests (ROI) of the grain in the isolated sample LM2 as shown in Figure 11.

Atomic fraction (%)	**ROI 1**	**ROI 2**
O[a]	36.6	30.4
Si[b]	2.4	6.3
P[b]	0.3	0.7
S[b]	0.8	0.9
Cl[b]	0	0
K[b]	0	0.1
Ca[b]	0.1	0.6
Ti[b]	0	0
Mn[b]	0	0
Fe[b]	18.8	12.6
Zn[b]	0.7	2.1
As[b]	0	0
Pb[b]	0.2	0.2
Fe/O atomic ratio	0.51	0.42

[a] Error on O is ± 5%

[b]Error on these elements is comprised between 1 and 5% when the atomic fraction is lower than 1%, elsewhere the error is lower than 1%.

Table 6. Quantitative elementary results obtained by µ-PIXE and µ-RBS on five regions of interests (ROI) of the grain in the isolated sample LM2 as shown in Figure 12.

Atomic fraction (%)	**ROI 1**	**ROI 2**	**ROI 3**	**ROI 4**	**ROI 5**
O[a]	36.2	40.2	40	34.2	37.8
Si[b]	13.8	0.5	0.2	13.4	0.6
P[b]	0	0.5	0.1	0.2	0.1
S[b]	15.3	0.2	0.1	14.0	0.9
Cl[b]	0.2	0	0	0	0.1
K[b]	0.3	0	0	0.2	0
Ca[b]	2.2	0.3	0.2	1.7	0.1
Ti[b]	0.2	0	0	0.1	0
Mn[b]	3.0	0	0	2.0	0
Fe[b]	3.8	18.1	19.0	4.6	17.2
Zn[b]	7.5	0.2	0.1	6.5	0.1
As[b]	0	0.1	0	0	0
Pb[b]	0.8	0	0	0	0
Fe/O atomic ratio	-	0.45	0.48	-	0.46

[a] Error on O is ± 5%

[b]Error on these elements is comprised between 1 and 13% when the atomic fraction is lower than 1%, elsewhere the error is lower than 1%.

Figure 1

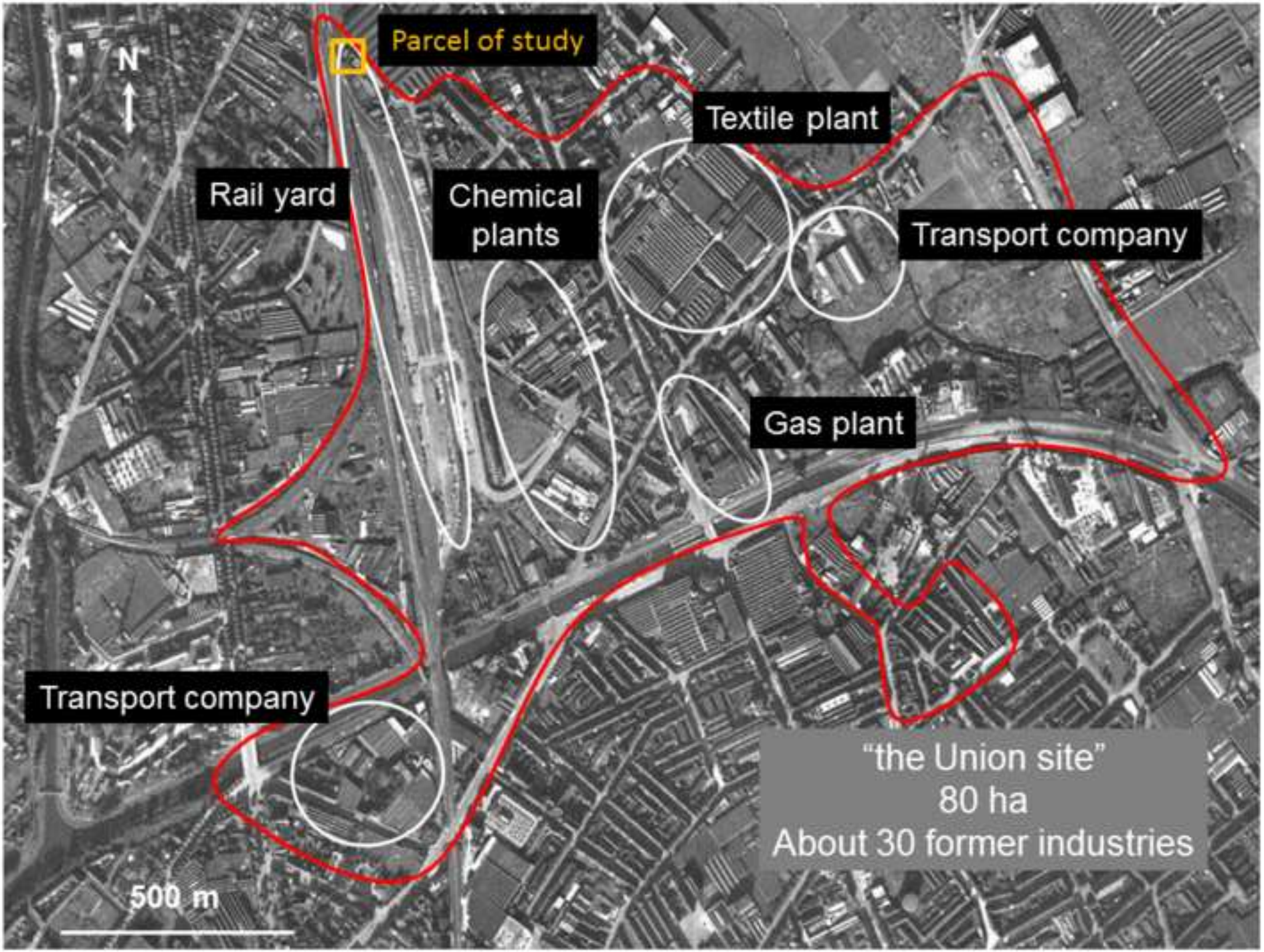
N
Parcel of study
Textile plant
Rail yard
Chemical plants
Transport company
Gas plant
Transport company
"the Union site"
80 ha
About 30 former industries
500 m

Figure 2

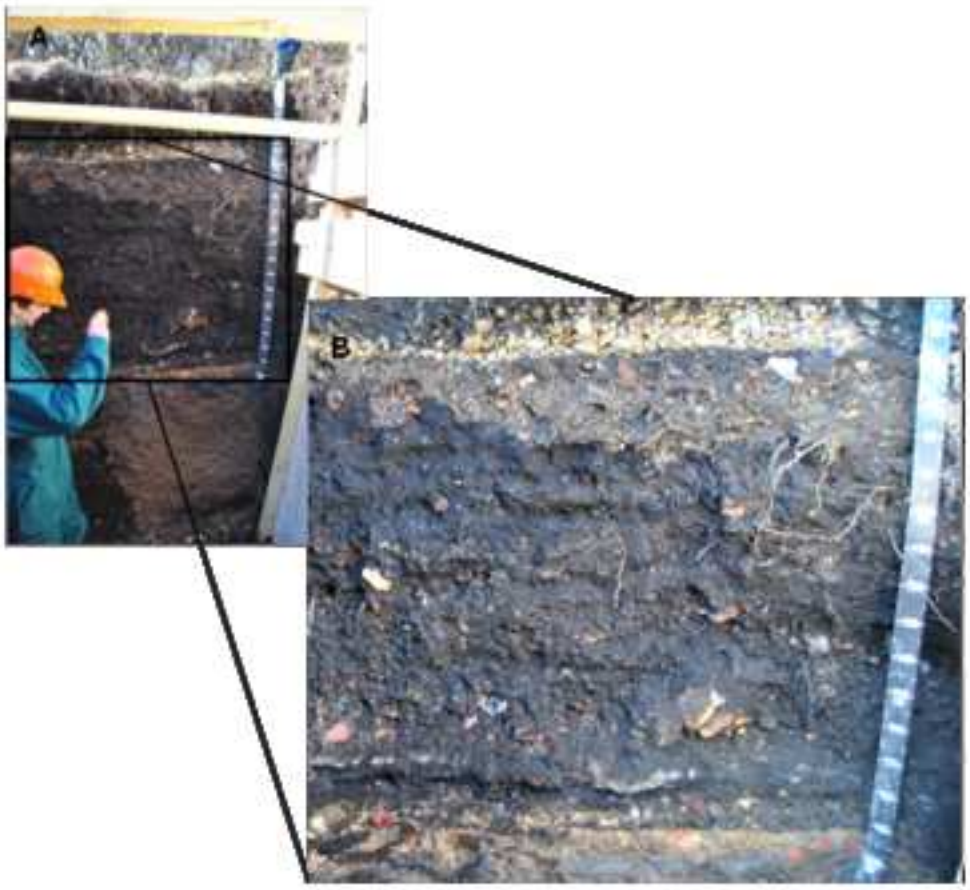
A
B

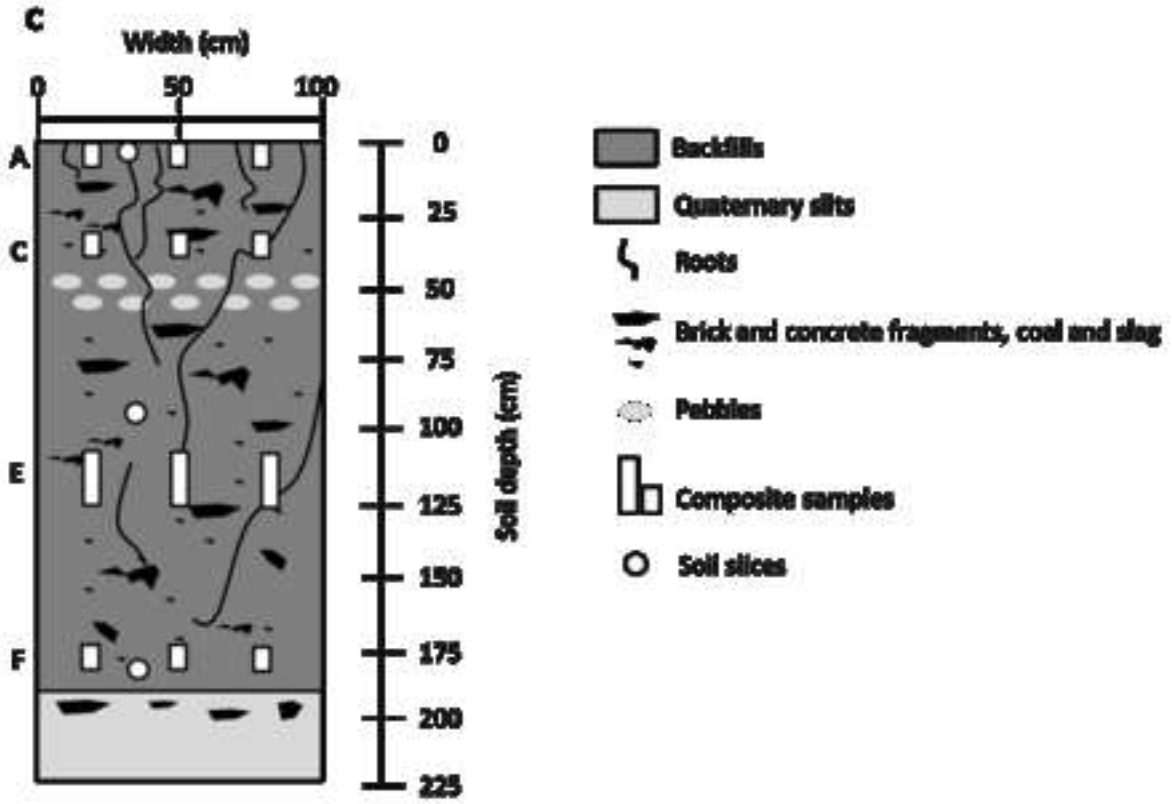
C
Width (cm)
0
50
100
A
C
E
F
0
25
50
75
100
125
150
175
200
225
Soil depth (cm)
Backfills
Quaternary silts
Roots
Brick and concrete fragments, coal and slag
Pebbles
Composite samples
Soil slices

Figure 3

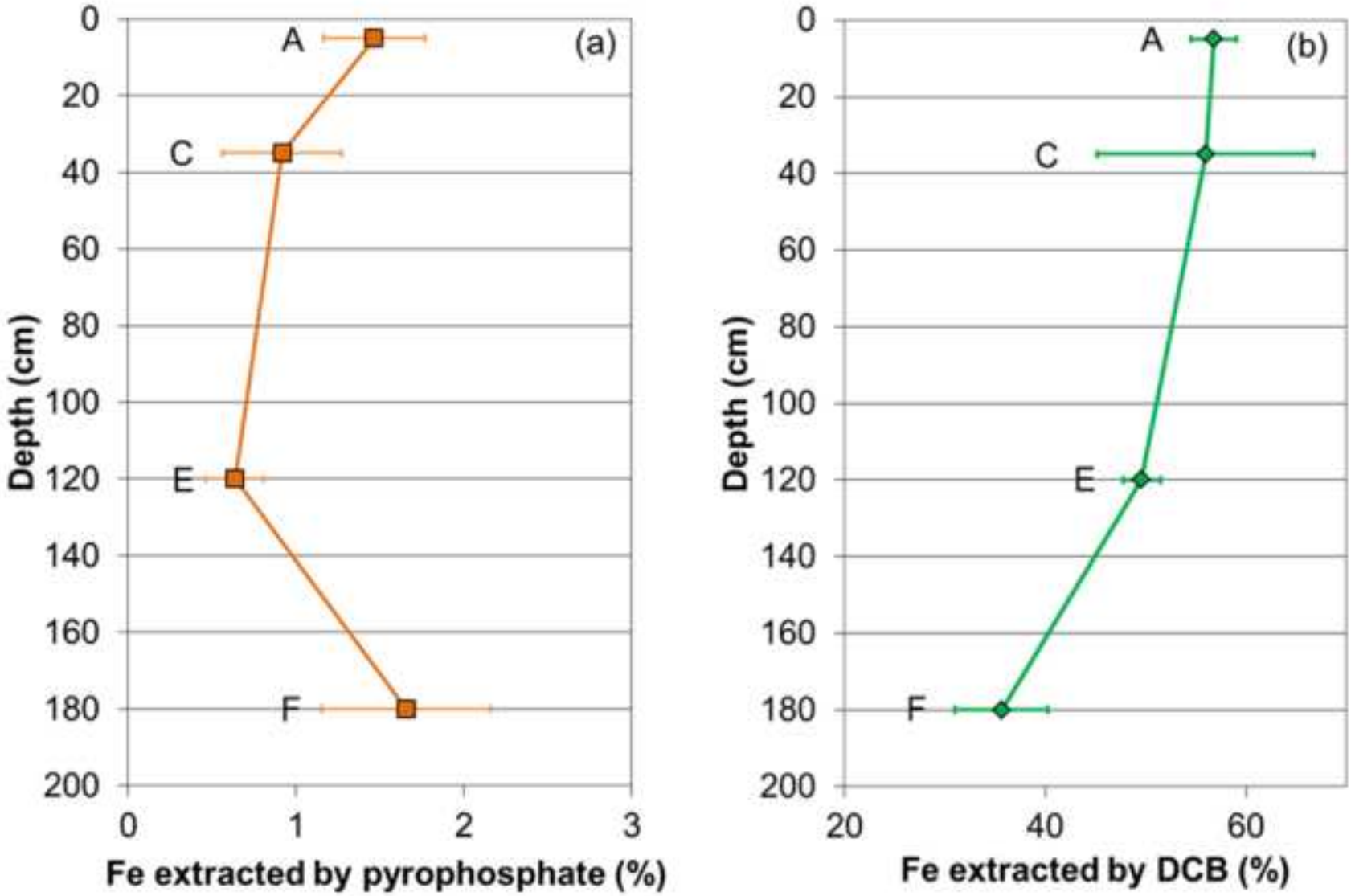
(a)
A
C
E
F
Depth (cm)
0
20
40
60
80
100
120
140
160
180
200
0
1
2
3
Fe extracted by pyrophosphate (%)
(b)
A
C
E
F
Depth (cm)
20
40
60
Fe extracted by DCB (%)

Figure 4

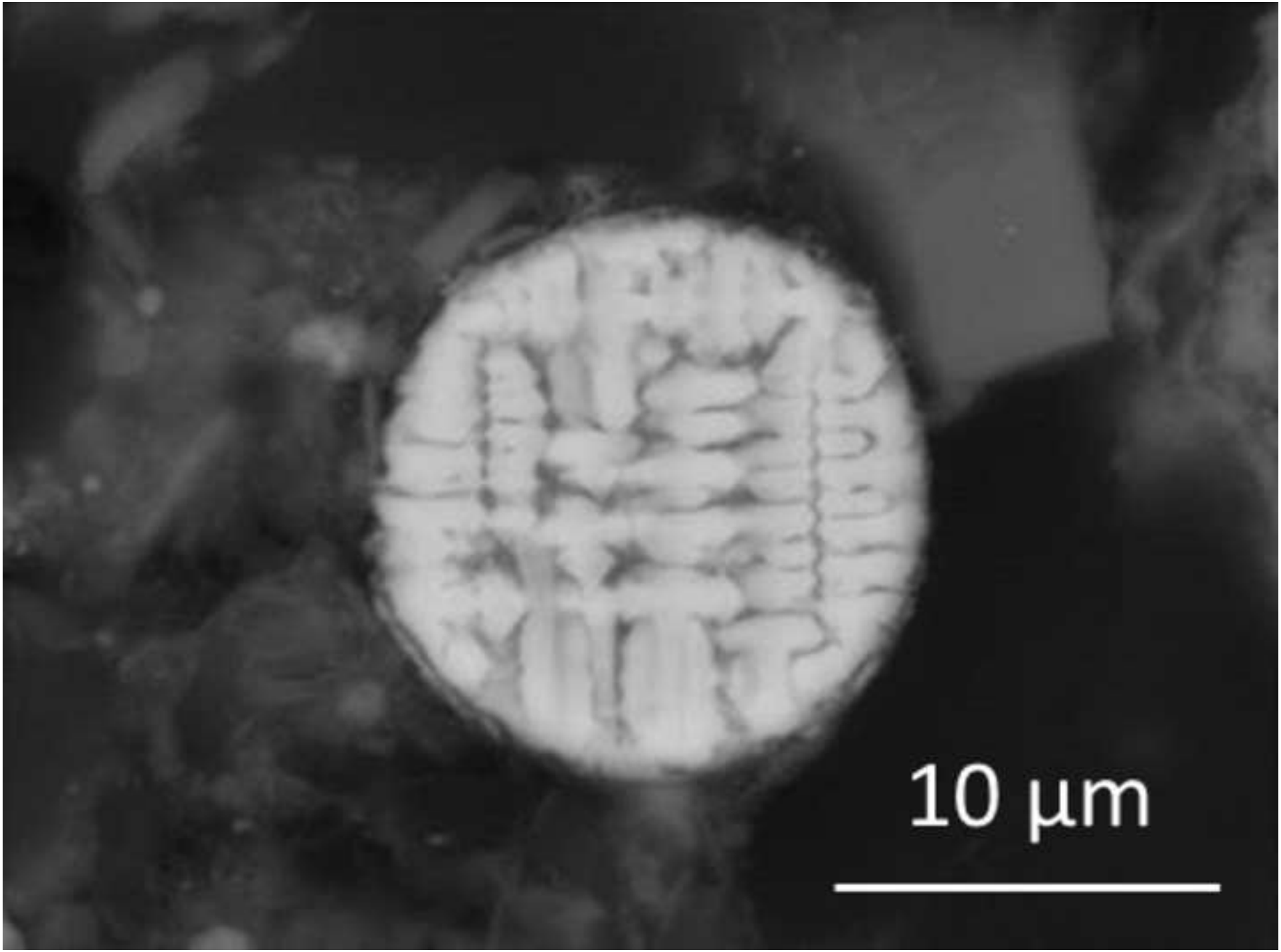

Figure 5

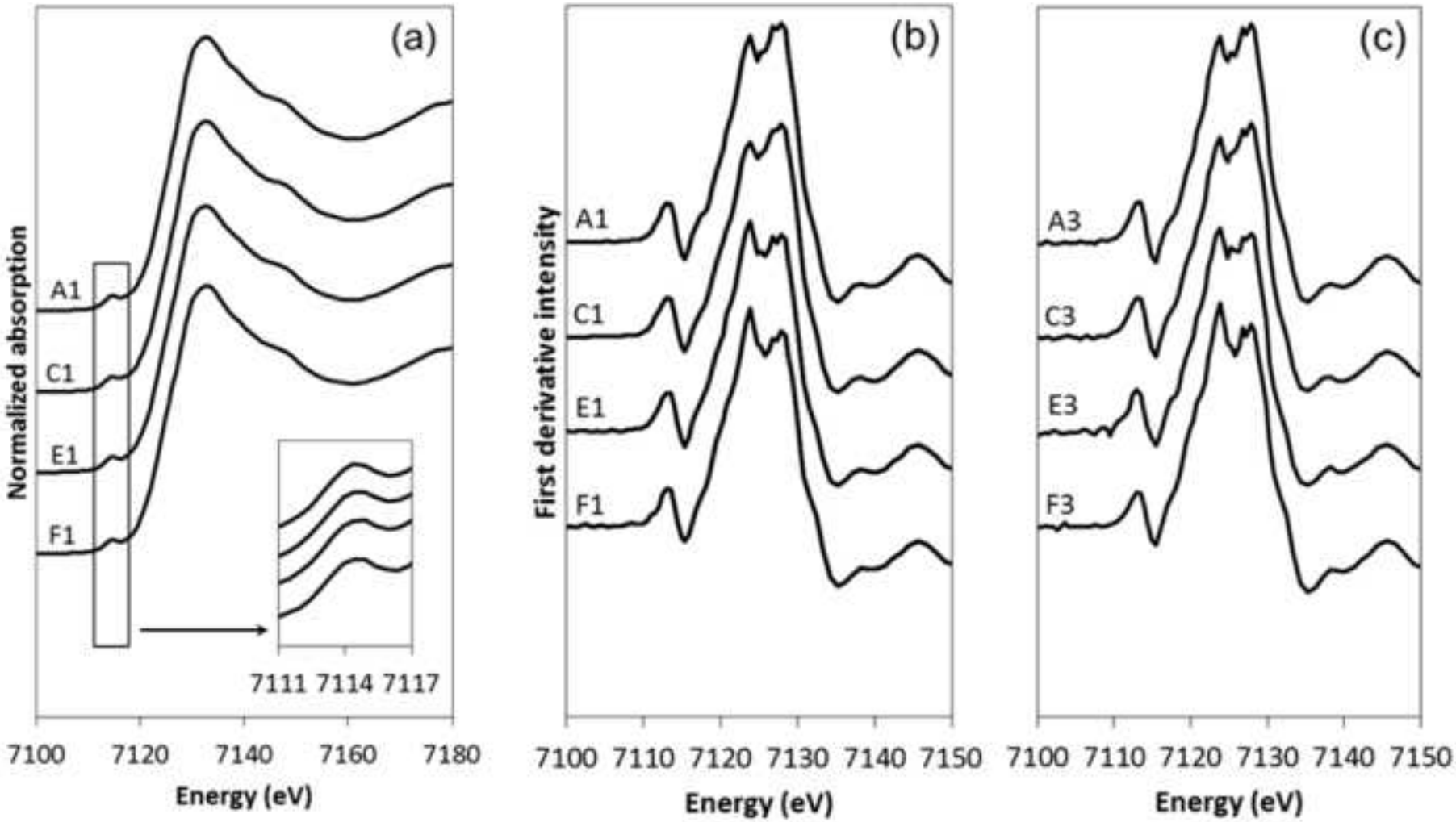
(a)
Normalized absorption
A1
C1
E1
F1
7111 7114 7117
7100 7120 7140 7160 7180
Energy (eV)
(b)
First derivative intensity
A1
C1
E1
F1
7100 7110 7120 7130 7140 7150
Energy (eV)
(c)
A3
C3
E3
F3
7100 7110 7120 7130 7140 7150
Energy (eV)

Figure 6

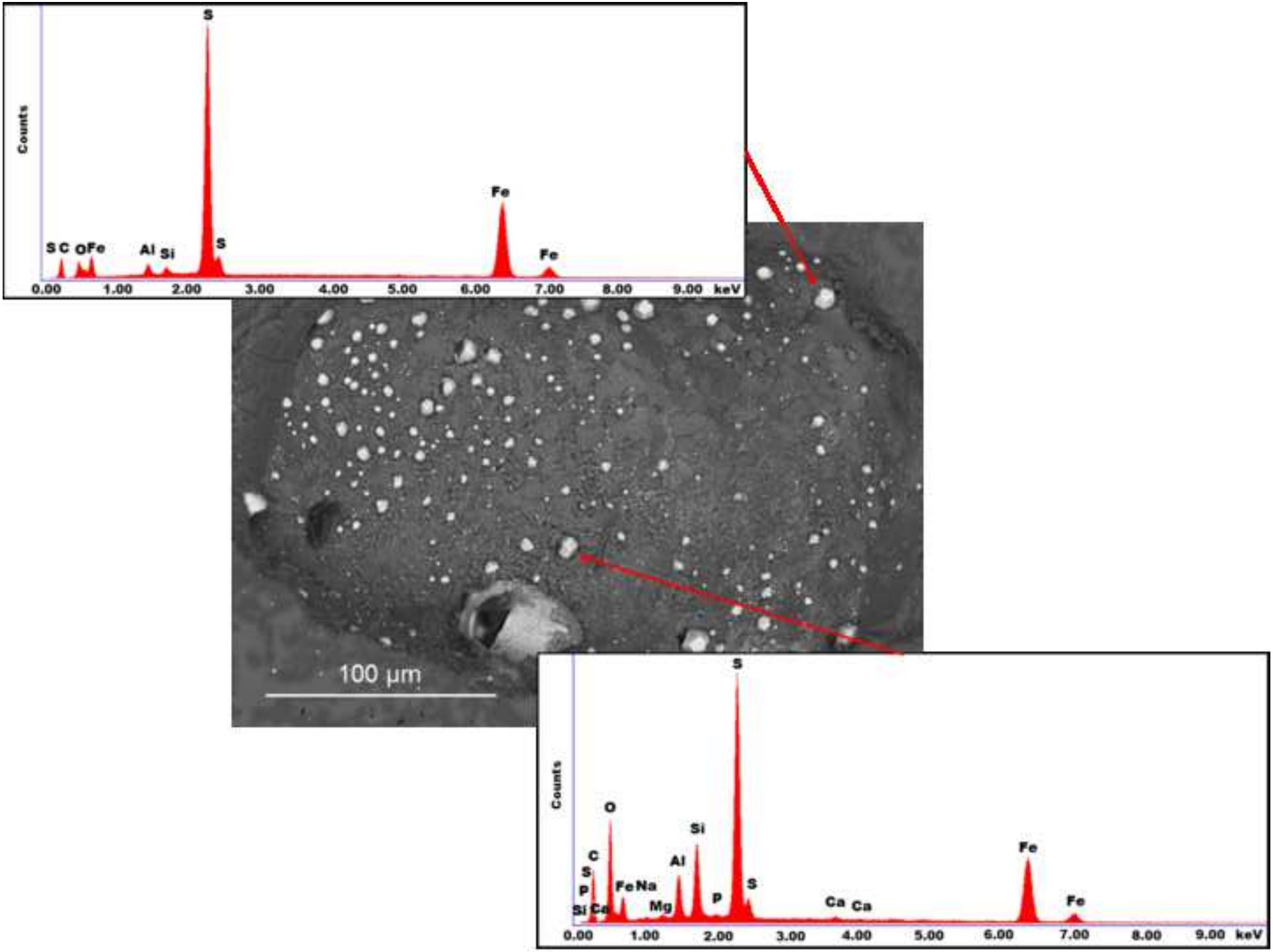
Counts
S
Fe
S C O Fe
Al Si
S
Fe
0.00 1.00 2.00 3.00 4.00 5.00 6.00 7.00 8.00 9.00 keV
100 µm
Counts
S
O
Si
C
Al
S
P
Fe Na
Mg
P
S
Si Ca
Ca Ca
Fe
Fe
0.00 1.00 2.00 3.00 4.00 5.00 6.00 7.00 8.00 9.00 keV

Figure 7

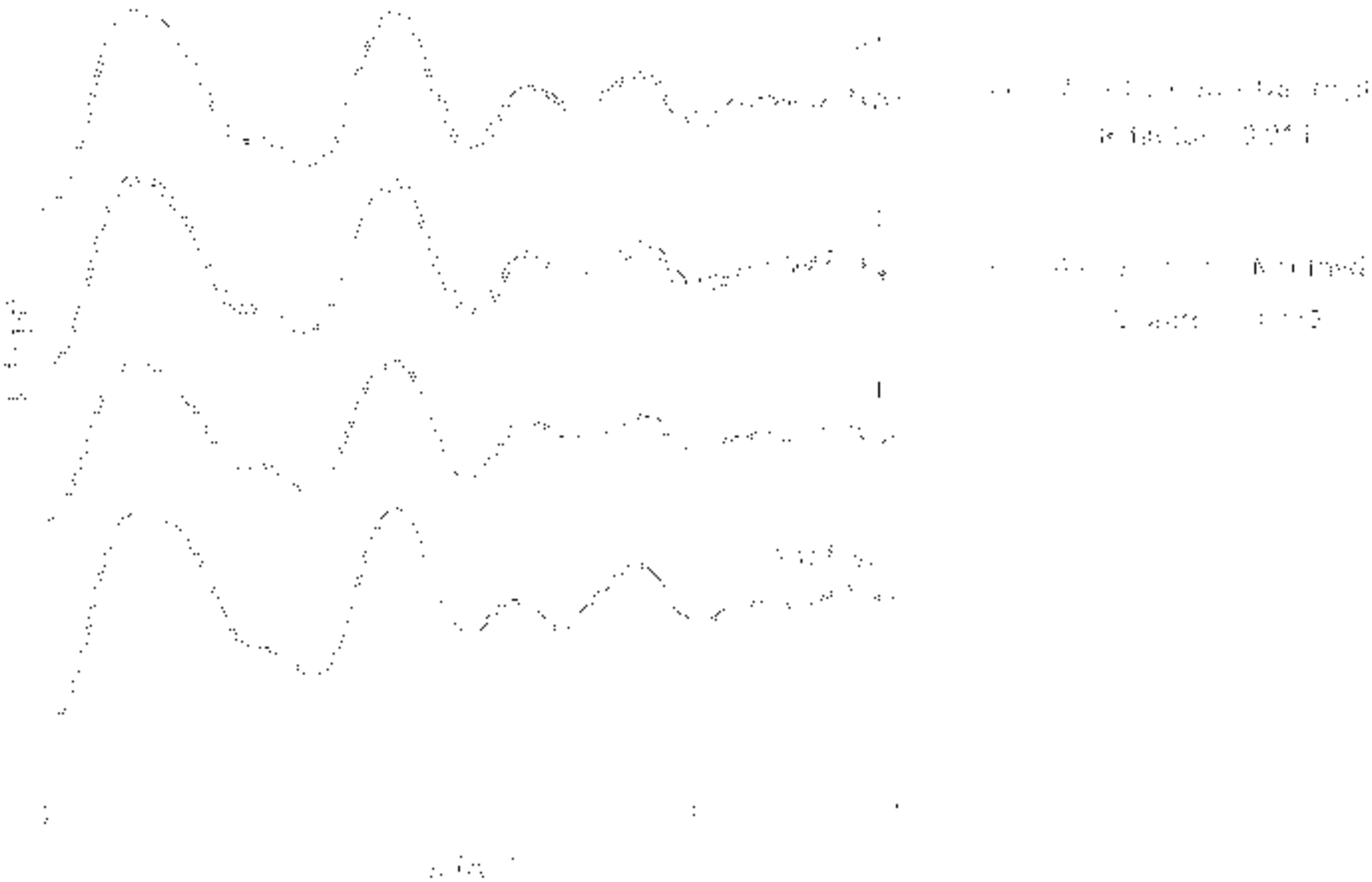

Figure 8

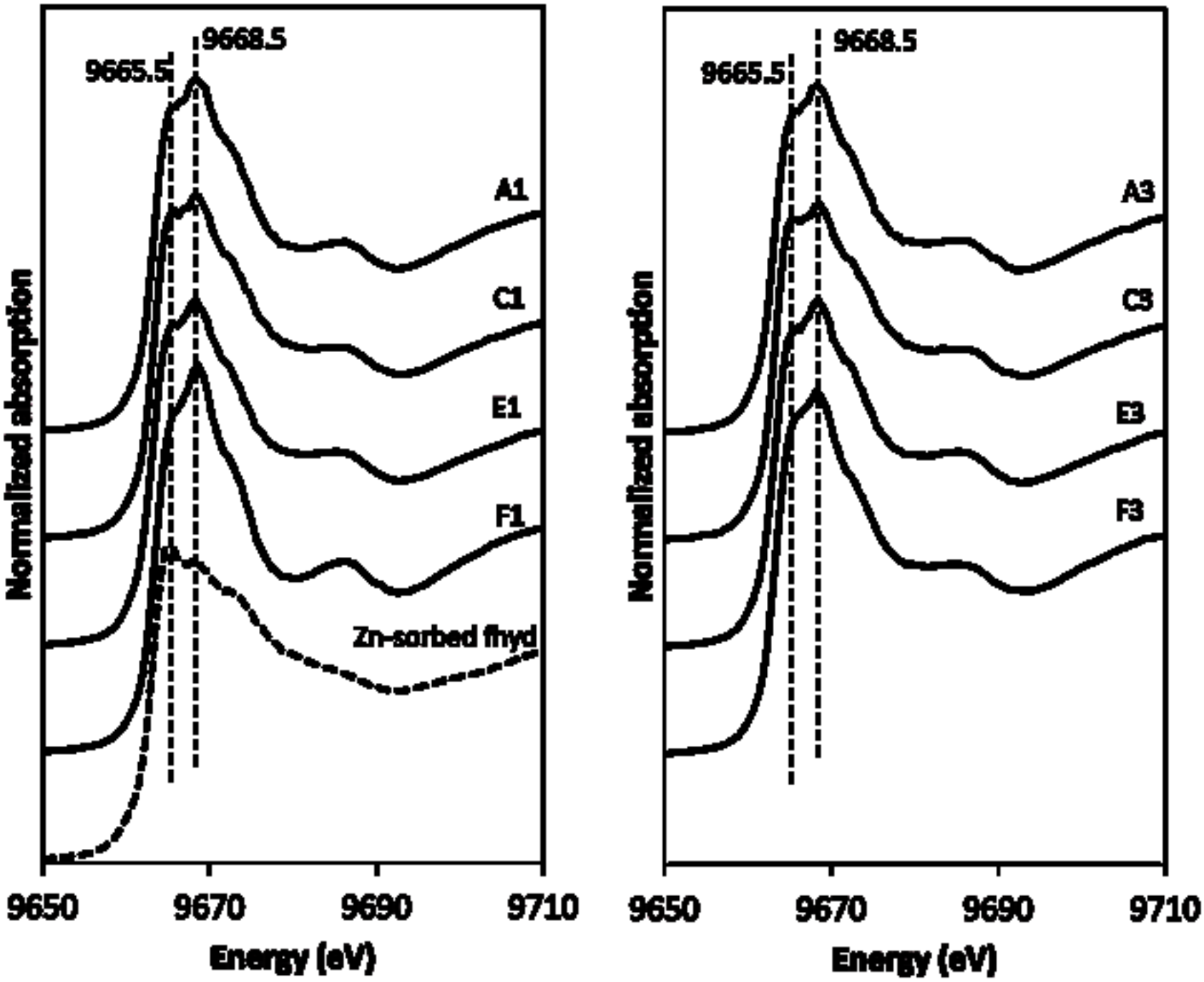
9668.5
9665.5
A1
C1
E1
F1
Zn-sorbed fhyd
Normalized absorption
9650
9670
9690
9710
Energy (eV)
9668.5
9665.5
A3
C3
E3
F3
Normalized absorption
9650
9670
9690
9710
Energy (eV)

Figure 9

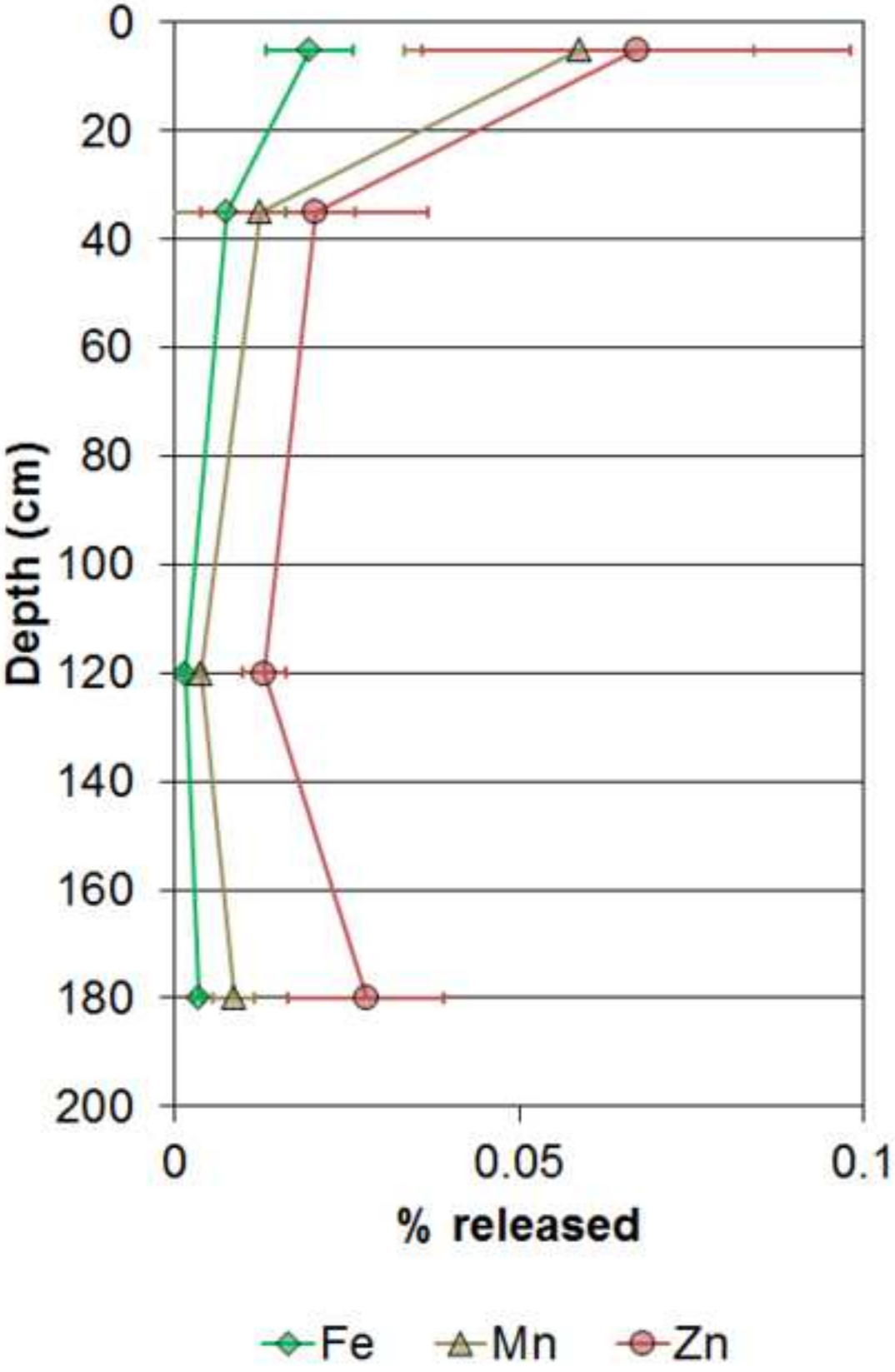
0
20
40
60
80
100
120
140
160
180
200
Depth (cm)
0
0.05
0.1
% released
Fe
Mn
Zn

Figure 10

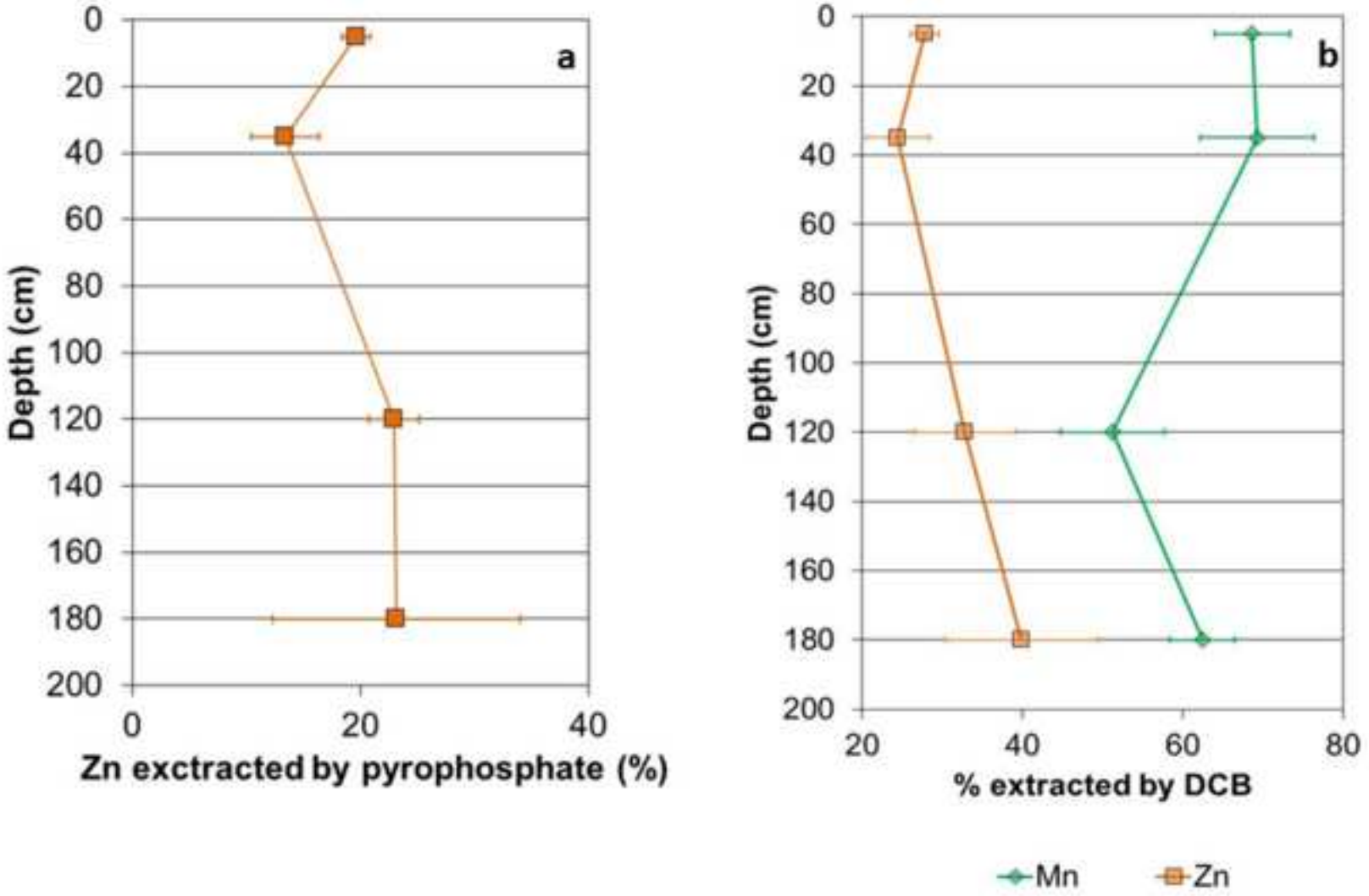
a
b
Depth (cm)
0
20
40
60
80
100
120
140
160
180
200
0
20
40
Zn exctracted by pyrophosphate (%)
20
40
60
80
% extracted by DCB
Mn
Zn

Figure 11

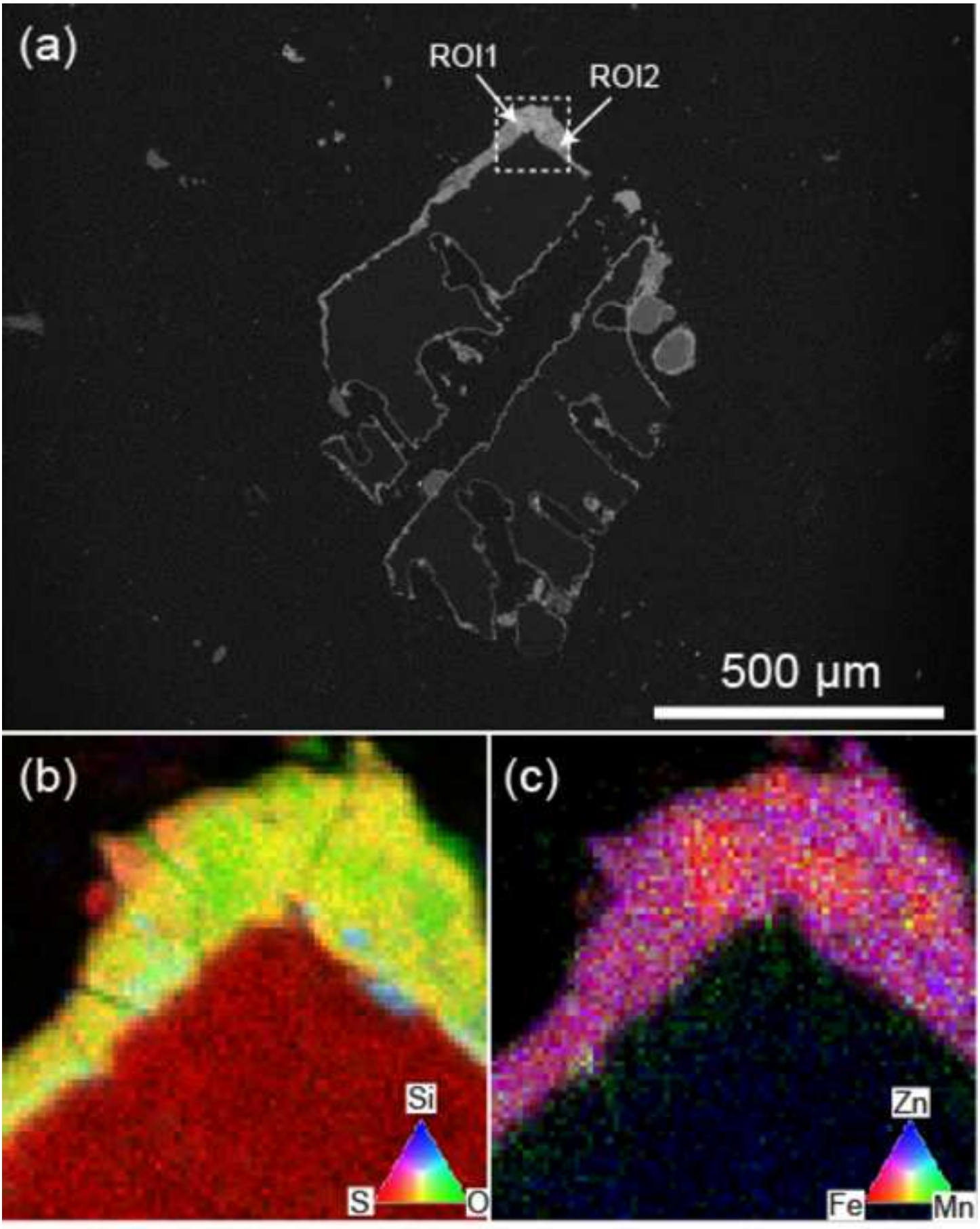

Figure 12

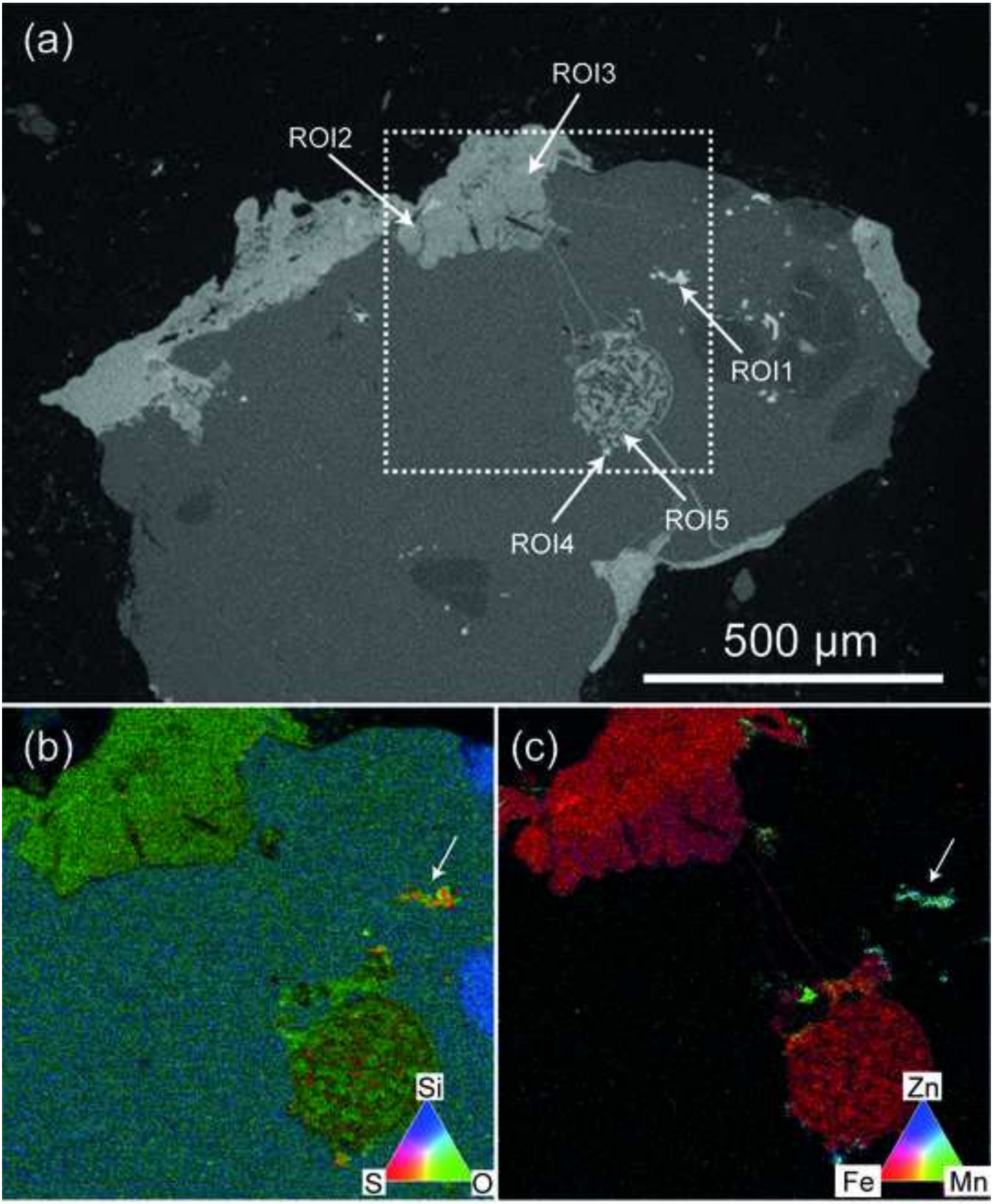

Figure captions

Figure 1. Aerial photograph (1951) of the Union site (red) and location of the main industries (white). The parcel of study is located in the orange square.

Figure 2. Soil profile. A General overview. B. Details of the central zone of the profile. C. Schematic representation of the soil profile.

Figure 3. Fe extracted by pyrophosphate (a) and DCB (b) throughout the soil profile (normalized by the total amounts in Fe of each sample).

Figure 4. Iron (hydr)oxide showing a texture of melting-quenching (in sample A1).

Figure 5. Fe-K edge XANES spectra (a) and corresponding first derivatives (b) and (c) of the composite samples from the Technosol profile located at the following range of depth: 0-10 cm (replicates A1 and A3), 30-40 cm (replicates C1 and C3), 110-130 cm (replicates E1 and E3) and 175-185 cm (replicates F1 and F3). For the replicate samples A3, C3, E3 and F3, only the first derivatives are given.

Figure 6. Fe-S bearing phases dispersed in a silicate mineral in the composite sample F1 (175-185 cm).

Figure 7. Least squares fit of EXAFS spectrum for A1 (0-10 cm, replicate N°1) and E1 (110-130 cm, replicate N°1) composite sample with a combination of ferrihydrite reference (Nat fhyd) and F1 composite sample (175-185 cm, replicate N°1).

Figure 8. Zn-K edge XANES spectra of the composite samples from the Technosol profile for two sets of replicate samples located at the following range of depth: 0-10 cm (replicates A1and A3), 30-40 cm (replicates C1 and C3), 110-130 cm (replicates E1 and E3) and 175-185 cm (replicates F1 and F3)., and Zn-K edge XANES spectra of Zn-sorbed ferrihydrite reference sample.

Figure 9. Fe, Mn and Zn released by leaching (% extracted from the total Fe, Mn and Zn content).

Figure 10. a. Zn extracted by pyrophosphate throughout the soil profile (normalized by the total amounts in Zn of each sample).b. Mn and Zn extracted by DCB throughout the soil profile (normalized by the total amounts in Mn and Zn of each sample).

Figure 11. Quantitative elemental mapping showing distribution of Si, S and O (map b) and Fe, Zn and Mn (map c) of a selected grain in LM2.

Figure 12 Quantitative elemental mapping showing distribution of Si, S and O (map b) and Fe, Zn and Mn (map c) of a selected grain in LM2. The white arrow in maps b and c indicate a specific Zn, Fe, Mn and S bearing phase.

Plates

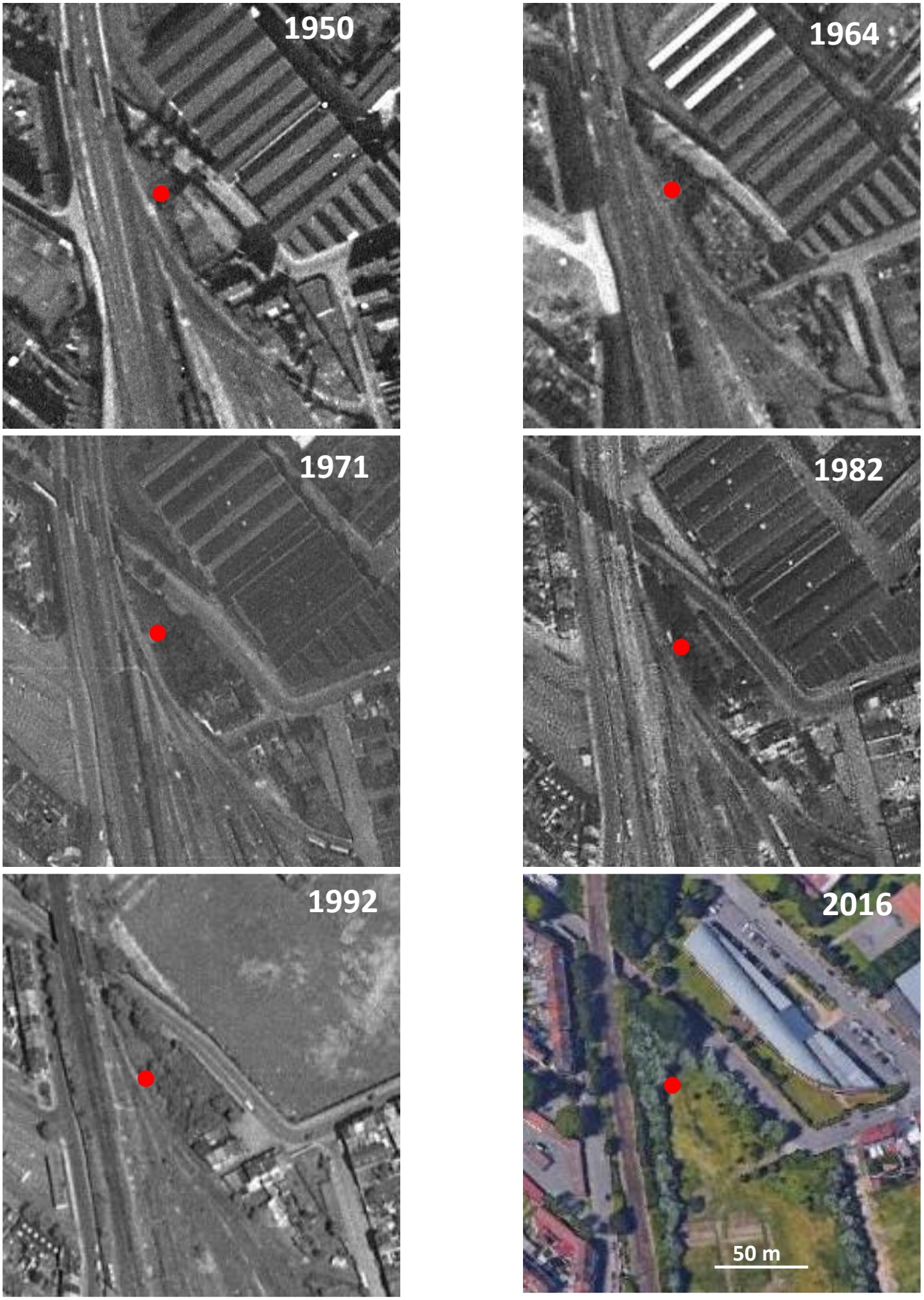

Study of aerial photographs between 1950 and 2016. The red dot indicates the location of the chosen pit.